Thermodynamic Scaling of Supersonic Retropropulsion Flowfeilds

Elliot Jennis

A thesis
submitted in partial fulfillment of the
requirements for the degree of

MASTER OF SCIENCE

University of Washington

2022

Committee:

Owen J. H. Williams

Carl Knowlen

Program Authorized to Offer Degree:
William E. Boeing Department of Aeronautics and Astronautics

University of Washington

Abstract

Thermodynamic Scaling of Supersonic Retropropulsion Flowfeilds

Elliot Jennis

Chair of the Supervisory Committee:
Owen J. H. Williams
Department of Aeronautics & Astronautics

The scaling of steady supersonic retropropulsion shock position and curvature is experimentally examined for a series of conical nozzles at the end of a cylindrical forebody at zero angle of attack. An experimental apparatus was constructed that for the first time allowed the influence of gas molecular weight, temperature and ratio of specific heats to be examined in addition to thrust, pressure, and mass flow ratees. It is revealed that the shape of the bow shock is close to self-similar regardless of gas composition and jet Mach number. In contrast to earlier studies, that suggest that thrust coefficient scales shock standoff distance, we find an additional dependence on the jet to freestream Mach number ratio, the product of which was found to collapse shock standoff distance data. In addition, explicit functions of gas molecular weight, temperature, ratio of specific heats derived from control volume analysis were found to scale the mass flow rate ratio and collapse the current dataset equally well for our data. Mach number ratio was also used to collapse the data but was not explicitly supported from the same control volume analysis. Additional comparisons to higher freestream Mach number data from the literature suggest the mass flow rate scaling is slightly superior, however further study is needed to determine scaling sensitivity to freestream Mach number and small geometric differences.

TABLE OF CONTENTS

LIST OF FIGURES

NOMENCLATURE

A: Area

a: Speed of sound

Ar: Argon

β: Ballistic Coefficient

C_D: Drag coefficient

CO_2: Carbon Dioxide

C_T: Thrust coefficient

D: Diameter

H: Shock standoff distance

He: Helium

M: Mach number

m: Mass

$\dot{m}$: Mass flow rate

MW: Molecular Weight

n: Refractive index

N_2: Nitrogen

p: Pressure

q: Dynamic pressure

R: Radius of curvature

Re: Reynolds number

T: Temperature

γ: Specific heat ratio

ρ: Density

U: Velocity

Subscripts

b: forebody

d: Dead-Air

e: Jet exit plane

j: Jet

∞: Freestream

0: Stagnation

2: Post bowshock

$*$: Condition at throat

ACKNOWLEDGMENTS

Finishing this thesis would not have been possible without the help and guidance of Owen Williams. During so many of the challenges faced during my time here be they related to research, my career, or personal issues, he seemed to drop everything to help me. When speaking with many of his students, that is an experience we all share. After two years I am still at a loss at how he can provide such individual attention to those under his wing while balancing a productive research and manuscript writing schedule in addition to all the family time he so clearly values. Truly he provides an example for his students to aspire to.

I would also like to thank my brother and sister in arms Hariprasad Annamalai and Lauren Jones. The countless late nights and early mornings spent prepping for exams and last minute homework submissions were made more than bearable by the friendship I have with the two of you. I owe many successes to you both including passing grades thanks to your patience and help, as well as the quality of this thesis to the assistance given in preparing and running experiments. Thank you for being there with me in the trenches through it all.

Finally, I would like to thank my partner and companion Haley. Without your support and constant encouragement I do not know where I would be.

DEDICATION

For my mother and father

Chapter 1

INTRODUCTION

One of the riskiest and most dramatic phases of spaceflight is Entry Descent and Landing (EDL). This period refers to the phase of flight when a spacecraft interfaces with a planetary body's atmosphere after spending a period of time in the vacuum of space. Broadly speaking, it can be characterized into three phases corresponding to three different fluid dynamic regimes. The entry phase corresponds to a hypersonic flight regime where rarefied gas dynamics and the transition to continuum flow are the dominant physics. This phase is typically where peak deceleration and heating occurs for the spacecraft and its payload. The descent phase falls into the supersonic flight regime. Under typical conditions this phase is where parachutes are deployed to further decelerate the descent vehicle. The final phase is landing which occurs at subsonic speeds. Parachute based deceleration has been the tried and tested method for the supersonic phase of EDL for decades. However, with the rise of booster return and the accelerated interest in human scale missions to Mars, vehicles are becoming too massive to rely effectively on parachutes alone. New technologies for decelerating spacecraft are needed to keep up with continual advances being made in the spaceflight industry.

This thesis focused on addressing key issues in the development of one of the most promising new EDL technologies, Supersonic Retropropulsion (SRP) [10]. SRP uses retrorockets to decelerate spacecraft during the supersonic phase of reentry. A major challenge with its development involves relating subscale test results to the performance of full scale vehicles. The complexity of the flowfields produced by SRP necessitates similarity parameters that go beyond traditional Mach number and Reynolds number matching often used in wind tunnel testing. A series of novel experiments were conducted to test new similarity param-

eters derived from first principles using control volume analysis. These experiments used a variety of gasses to simulate freestream and retrorocket exhaust flows at range of different temperatures, Mach numbers, and vehicle geometries.

1.1 Motivation

The two most commonly referenced applications for SRP include rocket booster return and sending high mass (10s of tons) payloads to the surface of Mars [11]. Successful use of SRP, for the purposes of booster return, has been demonstrated in the private sector by SpaceX, but remains poorly understood particularly when it comes to relating subscale testing to full scale flight conditions. For high mass Martian payloads, vehicle development cannot be rapidly iterated and destructively tested using full scale prototypes. These attributes were a key part in SpaceX's ability to overcome the challenges of successfully implementing SRP on the Falcon 9.

Current EDL systems in use on NASA's robotic Mars missions rely on supersonic parachute systems and blunt body configurations to slow payloads from hypersonic speeds in the upper Martian atmosphere to subsonic speeds near the surface. Mathematically, the effectiveness aerodynamic drag has on decelerating a vehicle is defined by its ballistic coefficient (equation 1.1) where m represents the mass of the object, C_D represents the drag coefficient, and A represents the cross-sectional area.

$$\beta = \frac{m}{C_D A} \tag{1.1}$$

A higher value for ballistic coefficient indicates a greater amount of energy needed to slow down a vehicle. Parachute technology is reaching physical limitations for effectively decelerating existing payloads on Mars due in part to the high ballistic coefficients of modern Mars missions. At the theorized ballistic coefficients required for a crewed Mars mission, such a mission would not survive reentry on the use of supersonic parachutes alone [12, 13]. One way to mitigate this problem is by increasing the drag coefficient (C_D) of a given spaceflight vehicle through the use of SRP. The additional retropropulsive force from SRP increases the drag coefficient at high thrust values, and redefines C_D as the sum of the aerodynamic drag

and the propulsive thrust from SRP (equation 1.2) [12, 13] in turn lowering the ballistic coefficient.

$$C_{D,Total} = C_D + C_T \tag{1.2}$$

Additional benefits from the use of SRP are highlighted in NASA's 2015 Technology Roadmaps. In this document, SRP has been listed as a high priority low TRL technology and an essential component in sending humans to Mars [10]. These benefits include the simplicity of implementing SRP allowing the use of off-the-shelf components for differently scaled missions, and the versatility of SRP due to its ability to function as a decelerator and course correction device from flight regimes in the upper atmosphere all the way to touchdown mitigating the technical risk associated with its development.

1.2 Objectives

The main purpose of this thesis is addressing the issue of relating subscale wind tunnel results to full scale conditions through the use of similarity parameters. Flow conditions in SRP interactions are characterized by many different variables including Mach number (M_∞ and M_e), Reynolds number (Re_∞ and Re_j), thrust coefficient (C_T), pressure ratio of the nozzle exit and post shock stagnation pressures ($\frac{P_e}{P_{0,2}}$), the molecular weights (MW_∞ and MW_j) and specific heat ratios of the gasses (γ_∞ and γ_j), as well as temperature of the gasses (T_∞ and T_j). This is a total of 12 variables assuming the jet and freestream flows are perfect gases while neglecting the effects of engine combustion and not taking into account geometric variation of the retrojet. Identifying the right parameter that can take into account the different effects these variables have on the flowfield has been a challenge for researchers. As a result, almost all previous experiments have employed cold-gas wind tunnel tests using either N_2 or air for both the freestream and jet gasses at approximately equal temperatures. These tests have questionable relevance in their results due to the lack of well defined similarity parameters that take into account thermodynamic variables. Work done for this thesis involved constructing an experimental apparatus capable of varying gas composition and temperature for the freestream and retrojet gasses with the aim of testing

additional scaling parameters that are theorized to account for the thermodynamic effects present in full scale SRP conditions.

The organization of this thesis first addresses where these proposed similarity parameters come from and how they are derived from first principles. A description of the experimental apparatus and its design process will follow. Additionally, in depth descriptions of data reduction and analysis will be included. Finally, the experimental results will be presented showing how variations in the chosen independent variables affect the scaling of the flowfield assuming self-similarity. The proposed similarity parameters will then be evaluated by how well they collapse the dataset and will be checked against historical and modern test results from outside sources to show generality.

Chapter 2

BACKGROUND & THEORY

2.1 Flowfield Topology

Most of the literature studying SRP focuses on configurations with one central nozzle along the center-line of the forebody [2]. Flowfields produced by configurations of this type have been shown to fall into into three different regimes depending on thrust and expansion conditions (see Figure 2.1) and are characterized based on how they affect the location of the standoff distance between the bow shock wave and the nozzle exit plane. Names for these regimes vary within the literature. Regime 1 is characterized by steady flow and low thrust. Curiously, vehicles operating in this regime have a lower drag coefficient than equivalent geometries with zero thrust. As thrust increases, regime 1 transitions to regime 2 which is characterised by a highly unstable flowfield. The transitional behavior between these regimes and its causes are still an active area of study. Shock flapping and jet penetration through the bowshock are two modes of instability present in this regime. In the literature, this regime is shown to have shock standoff distances many times greater than the forebody diameter of the test article [1, 3, 4, 14]. As thrust is increased further, a critical value is reached and the flowfield transitions to regime 3 where shock standoff distance dramatically decreases collapsing the flowfield down to a steady configuration. Once this regime is reached, features of the flowfield grow steadily in size, but remain stable with further increases in thrust. Many sources in the literature take regime 3 to be self-similar [3]. Regime 3 represents the conditions where SRP is applicable to the deceleration of spacecraft, and is where efforts to develop scaling laws have been focused. For regime 3 relevant conditions, the flowfield can be represented by Figure 2.2. Using the center nozzle configuration, the flowfield is axially symmetric. Starting at a streamline moving from right to left through the centerline of the

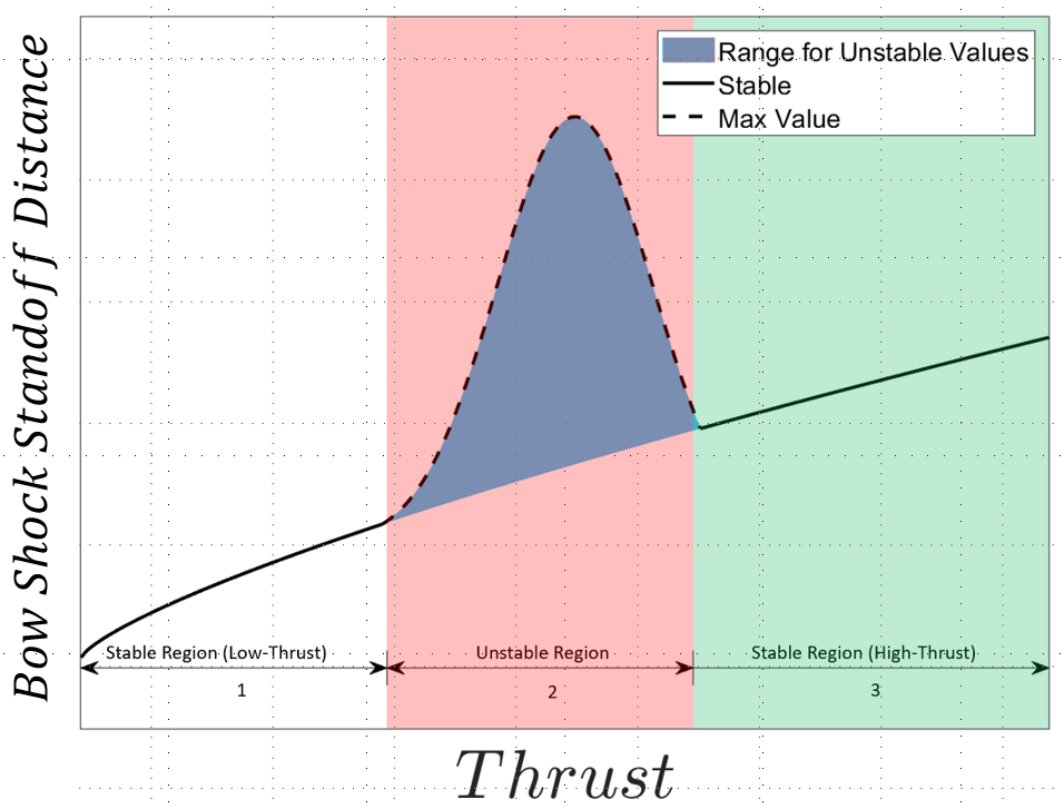

Figure 2.1: Simplified sketch depicting trends for normalized shock standoff distance as thrust increases. This cartoon captures the unstable region which forms between the high and low thrust stable regions. Within the unstable region are long-penetration shock oscillation instabilities. Lines are approximations meant to show trends rather than exact values (adapted from [1]).

supersonic jet, the retrojet gasses exit the retronozzle at Mach number M_e. This region of supersonic flow is bounded by a barrel shock and a shock structure referred to in Figure 2.2 as the Jet Terminal Shock. In the literature the Jet Terminal Shock is also called the Mach disk [7]. Once the jet fluid passes through the Jet Terminal Shock it becomes subsonic and the pressure in this region is assumed to increase iscentropically until it reaches a value equal to the pressure at the Free Stagnation point. From here, the jet fluid diverges away from the stagnation point and back towards the forebody. A streamline shown in Figure 2.2 is highlighted which marks the divide between the jet and freestream fluid. The location of this streamline is called the interface [4]. The jet fluid then travels into either a region known as the recirculation zone, or out and aft of the forebody. The recirculating zones are hypothesised to play a major role in causing the unstable flow phenomena associated with regime 2[2]. The pressure in this region is referred to as the dead-air pressure (p_d) and is used as the reference pressure to determine the expansion conditions of the jet [4, 7].

2.2 Scaling and Similitude

Full scale tests are not feasible when it comes to testing the performance of many aerospace vehicles due to the cost and complexity of doing so. The aerospace industry has relied on subscale testing for over a century to assess the flight characteristics of prototype vehicles without having to build full-scale versions to get around this problem. Challenges arise however, when drawing conclusions from subscale testing. It is not enough to simply match flight conditions with that of the full scale version as simply having a subscale model in those conditions will throw off the accuracy of results due to scaling effects. As a result, the field of dimensional analysis and the development of scaling laws seeks to identify testing conditions and procedures where subscale results will accurately predict the performance of the fullscale counterpart.

To date, all SRP studies have relied on CFD simulations or sub-scale physical testing to study its feasibility as a deceleration mechanism. The complexity of the interactions due to viscous forces in the shear layers between the freestream and plume flows as well as

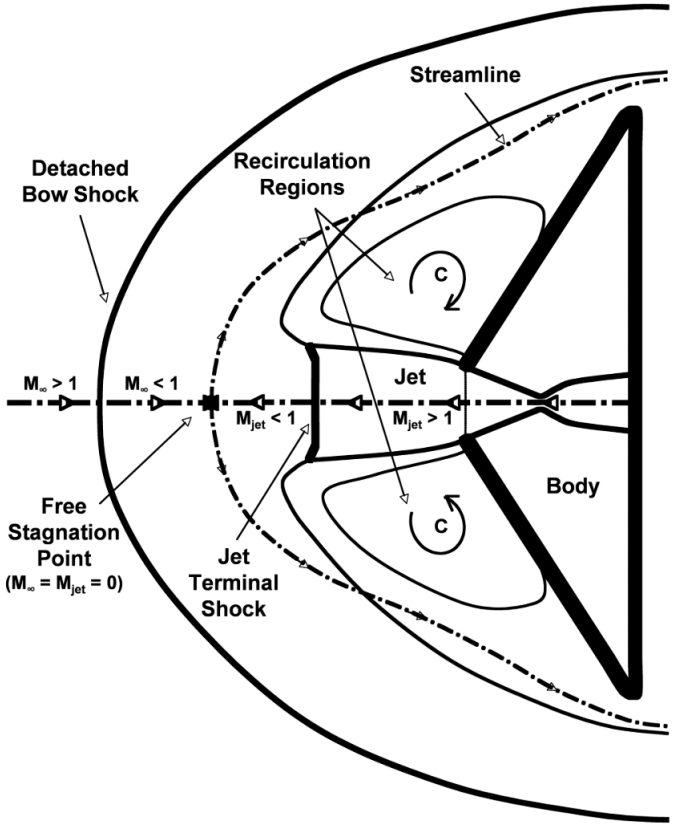

Figure 2.2: Simplified sketch of SRP flowfield structures for a central nozzle configuration under steady conditions (adapted from [2]).

the various shock structures inside the jet plume limits the effectiveness of simply matching Reynolds number, Mach number, and vehicle geometry for both the jet and the freestream for accurate subscale results. In many cases, attempting to match Reynolds number can be contradictory to achieving accurate thrust scaling required from momentum conservation making this task even harder [3]. Thankfully, literature studying SRP discounts the effects Reynolds number has on flowfield similarity due to the the drastic compressibility effects from Mach number variation within the flowfield compared to the relatively constant values for Reynolds number [9]. Additionally, effects driven by the shear layers are thought to be secondary mechanisms in SRP dynamics compared to the large discontinuities caused by the shock structures further discounting possible viscous effects [9].

Different similarity parameters have waxed and waned in perceived importance over the decades and the definitions of seemingly equivalent parameters change depending on the reference cited. This lack of consistency in both nomenclature and parameter definition within SRP literature has made studying scaling law development overtime quite challenging. Furthermore, effects of gas composition and temperature on the flowfield are very difficult to discern from existing data. While gas composition has been varied to a limited degree, useful data is scare. To the author's knowledge, temperature variation has not been investigated at all. A brief discussion on the development of these potential scaling laws and their definitions is important to understand the results presented later in this thesis. A summary of the test conditions and nozzle apparatuses used for each reference will be included at the end of this section in Table 2.1 and Figure 2.3.

The 1960s and 70s produced a broad variety of potential scaling laws for SRP flows as the U.S. government gained interest in studying retropropulsion as both a method for slowing the descent of interplanetary missions during EDL (with specific applications for the Viking missions) and as a mechanism for reducing drag and providing film cooling for hypersonic vehicles. The latter was referred to as stagnation point injection and received proportionally greater interest during this time due to the military applications of the technology.

Romeo and Sterret (1963) [1] were the first group to the author's knowledge to conduct a

robust study of SRP interactions as they related to vehicle deceleration at a broad range of flow conditions. They tested a flat faced cylinder with a single central nozzle at a constant freestream Mach number (M_∞) and varied the jet exit Mach number (M_e), jet pressure, and jet gas composition to a limited extent by testing N_2 as well as He jets. Unfortunately, the conditions used for the He tests led to highly unstable flowfields making any conclusions related to scaling between different gasses very challenging. They observed that the body to jet exit diameter ratio (D_b/D_e) as well as M_e influenced whether the flowfield became unstable for a given jet pressure [1].

Barber (1965) conducted a series of experiments in a continuous plasma tunnel capable of producing hypersonic freestream conditions for the purpose of investigating stagnation point injection. Various gasses including hydrogen and He were used in the retrojet for these experiments. Barber proposed a scaling parameter based on mass conservation denoted as $F * M_{12}^{\frac{1}{2}}$ which is defined in equation 2.1 as the relative mass flux ratio times the ratio of the molecular weights of the gasses.

$$F * M_{12}^{\frac{1}{2}} = \frac{\rho_j U_j}{\rho_\infty U_\infty} (\frac{MW_j}{MW_\infty})^{1/2} \tag{2.1}$$

Ultimately, the results showed that this term poorly scaled the shock standoff distance regardless of gas combination [15]. Interestingly however, the parameter was an effective term for scaling the heat transfer rate between the freestream and the test article [15].

Pindzola (1963) introduced scaling laws based on a variety of conservation principles including mass and momentum conservation. His report served more as a manual for properly conducting studies involving supersonic jets, rather than a research article, so a rigorous theoretical background of its claims is not present in the work, but his discussion of the different forms and uses of scaling laws is important. Pindzola organized his discussion based on the conservation law each term was derived from. All presented scaling parameters were developed using dimensional analysis to relate the freestream and jet flow conditions of the full-scale model to the subscale. For mass considerations, the ratio between the mass flow rates ($\dot{m}_j/\dot{m}_\infty$) of the jet and freestream was suggested as the principle scaling parameter.

After reorganizing the variables, the final parameter to be matched between the model and full-scale is shown below.

$$[\frac{A_j^2 P_j^2 \gamma_j^2 M_j^2 (RT)_\infty}{A_\infty^2 P_\infty^2 \gamma_\infty^2 M_\infty^2 (RT)_j}]_{model} = [\frac{A_j^2 P_j^2 \gamma_j^2 M_j^2 (RT)_\infty}{A_\infty^2 P_\infty^2 \gamma_\infty^2 M_\infty^2 (RT)_j}]_{full-scale} \tag{2.2}$$

Taking the square root of both sides of this equation and converting the gas constant to molecular weight gives the following equivalent relationship.

$$[\frac{A_j P_j \gamma_j M_j \sqrt{MW_j T_\infty}}{A_\infty P_\infty \gamma_\infty M_\infty \sqrt{MW_\infty T_j}}]_{model} = [\frac{A_j P_j \gamma_j M_j \sqrt{MW_j T_\infty}}{A_\infty P_\infty \gamma_\infty M_\infty^2 \sqrt{MW_\infty T_j}}]_{full-scale} \tag{2.3}$$

Additionally, a parameter defined as thrust coefficient (C_T in the reference, defined as C_F in this thesis) was introduced primarily to simulate momentum considerations between the model and full-scale as it was thought that momentum fluxes were the primary factor behind the shock structure locations within the flowfield [16]. Its definition is presented below.

$$C_F = \frac{F_j}{q_\infty A_\infty} \tag{2.4}$$

F_j is defined as the thrust of the jet which is determined by equation 2.5.

$$F_j = \rho_j U_j^2 A_j + (p_j - p_\infty) A_j \tag{2.5}$$

These two terms are very important as they form the basis for much of the rest of the experimental studies of SRP scaling.

Finley (1966) produced an in-depth theoretical analysis of the SRP flowfield and conducted a series of experiments to test his hypothesis. The work was done at extremely low thrust indicative of stagnation point injection applications. All of his experiments were conducted with a domed blunt body using a single central sonic nozzle. Only air-air interactions were investigated. Finley relied on a fairly complex control volume, which will be discussed in more detail in the next section, to derive the scaling parameters he thought best approximated the flowfield. By conducting a momentum balance using his control volume, Finley derived an equation for scaling the distance between the interface streamline (see previous

section on flowfield structures) and the nozzle exit plane normalized by the model body diameter shown in equation 2.6.

$$\frac{D_f}{D_b} = \sqrt{C_T[1 + \frac{V_l}{G_j} cos(\alpha)]Z^{-1}} \tag{2.6}$$

In this equation, thrust coefficient (C_T) is defined as the vacuum thrust coefficient represented by

$$C_T = \frac{\dot{m}_j U_j + p_j A_j}{q_\infty A_\infty} \tag{2.7}$$

The terms V_l and G_j are functions of M and γ for both the jet and the shear layers [4]. Z is primarily a function of α which itself is the angle at which the shear layer flow exits the control volume [4]. Calculating α from flow conditions was not possible so Finley relied on experimental results to find a rough approximation [4]. Data from experiments that varied the model body outer diameter showed that the major structures within the flow (bow shock, interference region, and jet shock) all scaled linearly with $C_T^{1/2}$. Unfortunately, given that that the Mach numbers for both the jet and freestream as well as gas composition for the jet and freestream were not varied left doubts as to whether this equation is generalizable. What this paper does show however, is that a candidate scaling law that captures all of the flowfield topology may potentially be defined as C_T multiplied by a function of M and γ.

Jarvien and Adams (1970) conducted a study using a geometry that was being considered by NASA for use in Martian reentry [14]. This study varied a wide variety of parameters, many of which (angle of attack and number of retrothrusters) are not relevant for this thesis. However, their findings regarding the bow shock location as a function of C_T are relevant. They saw that varying the freestream Mach number would affect the bow shock location when tested at a given value of C_T. This finding yields further credence to the development of a C_T based scaling law multiplied by a function of Mach number.

More recent attempts at understanding how these parameters affect SRP flowfields has been carried out due to the renewed interest in retropropulsion primarily caused by the rise in reusable boosters. Data collected in the early 2000s as well as more recent data from this decade has provided further insight into the problem of scaling.

Ashley Korzun's dissertation (2009) provides a very in depth analysis of the Finley derivation and attempted to apply it to supersonic jets using analytical methods. An iterative process was then used to calculate the flow turning angle α which was used as a convergence tool for the finite difference method used for her calculations. Korzun found that this process using Finley's equations underestimated the interface location by a significant degree. This finding has driven other researchers away from Finley's model in recent years, however, equations derived from his work are were shown to predict Mach disk location and diameter to a high degree of accuracy [2].

Korzun and Cassel (2020) wrote a survey of historical and modern SRP experimental results to bring together all the disparate scaling parameters suggested over the decades in one place. The addition of NASA's SRP test data collected at the Unitary Plan Wind Tunnel at the Ames facility [17] was also included in this report to provide a modern dataset for which the historical data could be compared to. The control volume they used was simplified compared to that of Finley (1966) in an attempt to derive an accurate scaling law from first principles [3]. This analysis suggested the introduction of parameters Ψ and Γ defined below.

$$1/\Psi = \frac{MW_j T_{0\infty}}{MW_\infty T_{0j}} \quad 1/\Gamma = \frac{\gamma_j}{\gamma_\infty} \tag{2.8}$$

These two parameters were derived from a rearrangement of $\dot{m}_j/\dot{m}_\infty$ and were suggested as key terms for scaling from one set of gas combinations to another. These terms are closely related to those presented in Pindzola (1963) but used total rather than static temperature. Unfortunately, the lack of usable data representing conditions other than air-air or N_2-N_2 and the geometric variation within their datasets makes evaluating their conclusions challenging. Compounding this issue is that existing He data is limited by a lack of stable cases at high C_T values [1, 14]. Furthermore, their results suggest that under-expansion of the jet and C_T values exceeding unity are requirements for flow similarity. The term used to approximate expansion conditions is the jet exit pressure to freestream post shock stagnation pressure ratio ($P_e/P_{0,2}$). Under-expansion is defined as $P_e/P_{0,2} > 1$. They freely admit however that geometric parameters like body to jet throat diameter ratio (D_b/D^*) have an independent

effect on the flowfield.

Recently, Gutsche et al (2021) collected data exploring the validity of using some of the parameters suggested by Korzun and Cassel. The paper used both wind tunnel data and CFD to test existing theories and extracted shock standoff distances as well as the distances to interface, Mach disk, and triple point. The experimental data used only air-air interactions with a relatively unique model geometry containing a stepped nozzle exit to OML transition. The range of M_∞ for their experiments varied between 5.3-7. Key flowfield structures were shown to have a linear relationship with $C_T^{1/2}$ and did not depend on M_∞ or M_e, within their error bars. It is possible that the high Mach numbers used in their tests reduced the effect M_e had on the relationship between C_T and shock standoff distance that was suggested by Korzun and Cassel [3].

There are many other historical and modern references that studied SRP flowfields, but the author believes those presented here are the most important for understanding scaling laws and how thermodynamic terms may be included in them. Parameters like C_T show promise, but there is still no clear consensus on its effectiveness when varying Mach number and no data has shown it to effectively scale different gas combinations. Additionally, C_T varies in definition from paper to paper with some sources using the vacuum thrust version and others sticking to the C_F version while still others drop the pressure terms all-together. mass flow rate scaling has been suggested as well, but a lack of data supporting its use makes confirming this hypothesis difficult. A final challenge is the variety of geometries used by different researchers. Gurche et al (2021) and Kozrun and Cassel (2020) both emphasize that geometry has a large effect on flow similarity and stability but cannot agree on which geometric ratio to use.

For clarity, subsequent references to geometric scaling will use D_b/D_e, and C_T will be defined as presented in equation 2.7. Additionally, the choice of a flat face, a conical face, or a stepped geometry greatly changes the local dead-air pressure and the circulation regions around the central jet barrel shock making the waters even murkier when comparing existing datasets [7, 14]. Choosing an extremely simple geometry like a flat faced cylinder can isolate

Reference	M_∞	M_e	C_T	Freestream	Jet	D_b/D_e
Romeo and Sterret [1]	6	1-10.3	0-7	Air	Air	2.25-57.7
Barber [15]	6-8	5, 8	0-6	Air	He, H_2, N_2	12.38
Finley [4]	2.5	1	0-0.16	Air	Air	7.58
Jarvinen and Adams [14]	0.4-2	3.2-4.7	0-40	Air	Air, He	5.65-11.3
Berry et al [17]	2.4, 3.5, 4.6	2.94	0-3	Air	Air	12
Gutsche et al [7]	5.29, 7.03	2.2, 2.44	1.5-4.2	Air	Air	5.48

Table 2.1: Collection of conditions for cited references using single central nozzle configurations.

these geometric effects from the inflow conditions which provided the motivation for choosing the test geometries used in this thesis. With this summary in place, a deeper dive into the candidate scaling laws investigated in this thesis will be presented in the next section.

2.3 Scaling Law Derivations

Attempts at deriving scaling laws for SRP flowfields have been made in the past using control volume (CV) analysis. Two examples are most commonly referenced in the literature; Finley's [4] and Korzun and Cassel's [3] CVs. Both attempt to derive an equation that relates a flowfield scaling parameter to a normalized interference region (A/A_b) that represents the area bounded by the fluid affected by the SRP interaction. Finley uses the interface streamline as the boundary of this area while Korzun and Cassel use the bow shockwave. Assuming the interference region shape is self-similar, this area can be put in terms of a standoff distance from the retronozzle tip creating a scaling law for SRP flows. Finley (1966) used a complex CV shown in Figure 2.5 and a momentum balance to derive a relationship between a function of thrust and the normalized standoff distance of the interface streamline (dashed line in Figure 2.2). Korzun and Cassel (2020) used a different more simplified CV

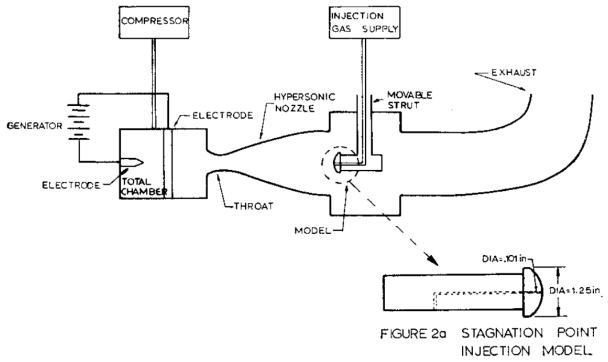

(a) Barber (1965) apparatus from [15].

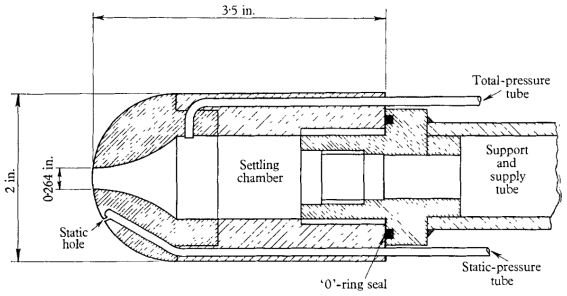

(b) Finley (1966) apparatus from [4]. Dimensions in inches.

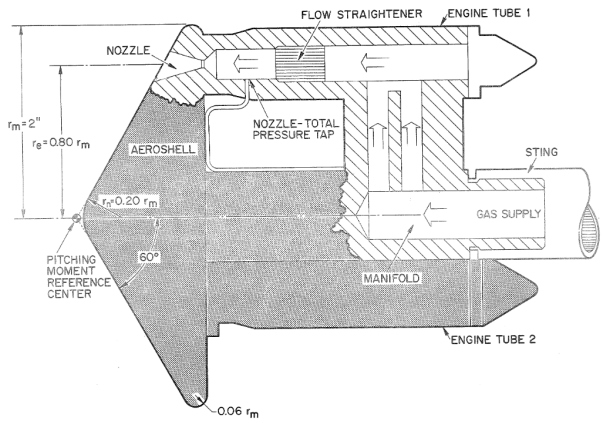

(c) Jarvien and Adams (1970) apparatus from [14]. Dimensions in inches.

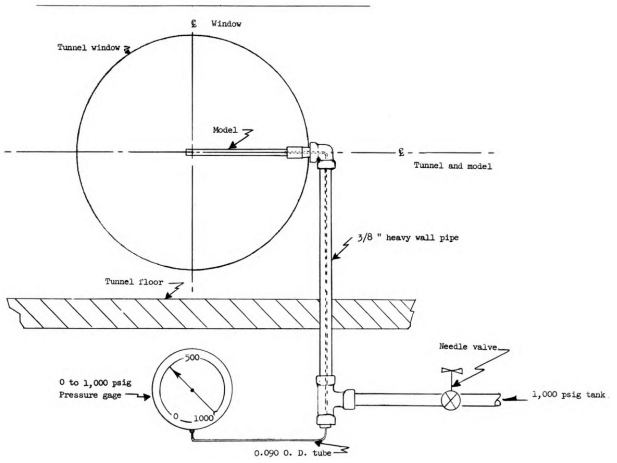

(d) Romeo and Sterret (1963) apparatus from [1].

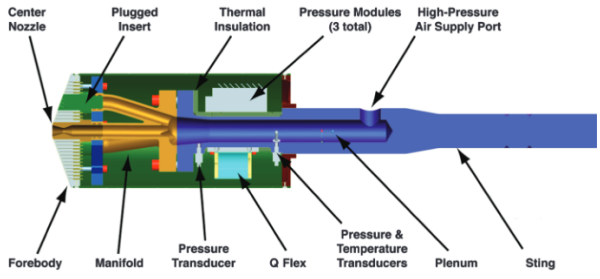

(e) Berry (2014) apparatus from [17].

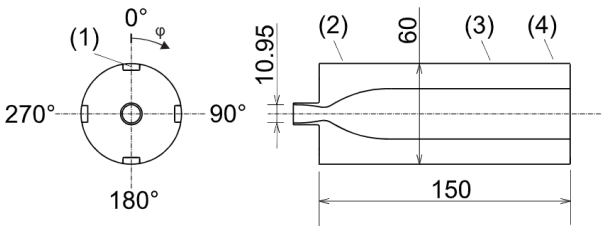

(f) Gutsche et al (2021) test model from [7]. Dimensions in millimeters.

Figure 2.3: Various types of test articles and sting apparatus used for historical and modern SRP experiments.

in their paper shown in Figure 2.4. They used both conservation of mass and momentum to derive their scaling law relationships. The use of conservation of mass vs momentum is indicative of author's preference rather than mathematical necessity. In this section, the derivations from both Korzun and Cassel (2020) and Finley (1966) respectively will be reproduced to a limited extent.

Beginning first with the derivation of Korzun and Cassel. A mass flow balance using the CV from Figure 2.4 is shown in equation 2.8 with inflow mass from the freestream and jet equaling the outflow mass in the mixed flow regions (denoted by subscript m). The density and velocity in the mixed regions is not known, therefor it is left as a function of radial distance from the central axis of symmetry (r). The boundary of the CV is represented by A with regions outside this area assumed to contain undisturbed freestream flow.

$$\rho_\infty U_\infty A + \rho_j U_e A_e = \int_{A_b}^{A} \rho_{m\infty}(r) U_m(r) dA + \int_{A_b}^{A} \rho_{mj}(r) U_m(r) dA \tag{2.9}$$

This balance is then normalized by $\rho_\infty U_\infty A_b$ to get equation 2.9.

$$\frac{A}{A_b} + \frac{\rho_j U_e A_e}{\rho_\infty U_\infty A_b} = \int_1^{\frac{A}{A_b}} [\frac{\rho_{m\infty}(r) + \rho_{mj}(r)}{\rho_\infty}] \frac{U_m(r)}{U_\infty} d(\frac{A}{A_b}) \tag{2.10}$$

Unfortunately, it is not possible to solve for the integral on the right hand side due to the unknown distributions in density and velocity [3]. The mass flow rate ratio can be moved to the right hand side yielding an equation that defines the nondimensionalized disturbance region caused by the bow shock wave in terms of mass flow rate ratio and the mixing region integral.

$$\frac{A}{A_b} = -\frac{\rho_j U_e A_e}{\rho_\infty U_\infty A_b} + \int_1^{\frac{A}{A_b}} [\frac{\rho_{m\infty}(r) + \rho_{mj}(r)}{\rho_\infty}] \frac{U_m(r)}{U_\infty} d(\frac{A}{A_b}) \tag{2.11}$$

Expanding the mass flow rate ratio term is achieved using two assumptions, ideal gas law, and iscentropic flow through the retronozzle. The density terms are replaced using the equation of state to introduce temperature and the gas constant R into the equation. By multiplying both sides by γ_j/γ_j and $\gamma_\infty/\gamma_\infty$ like-terms are combined to produce a speed of sound ratio

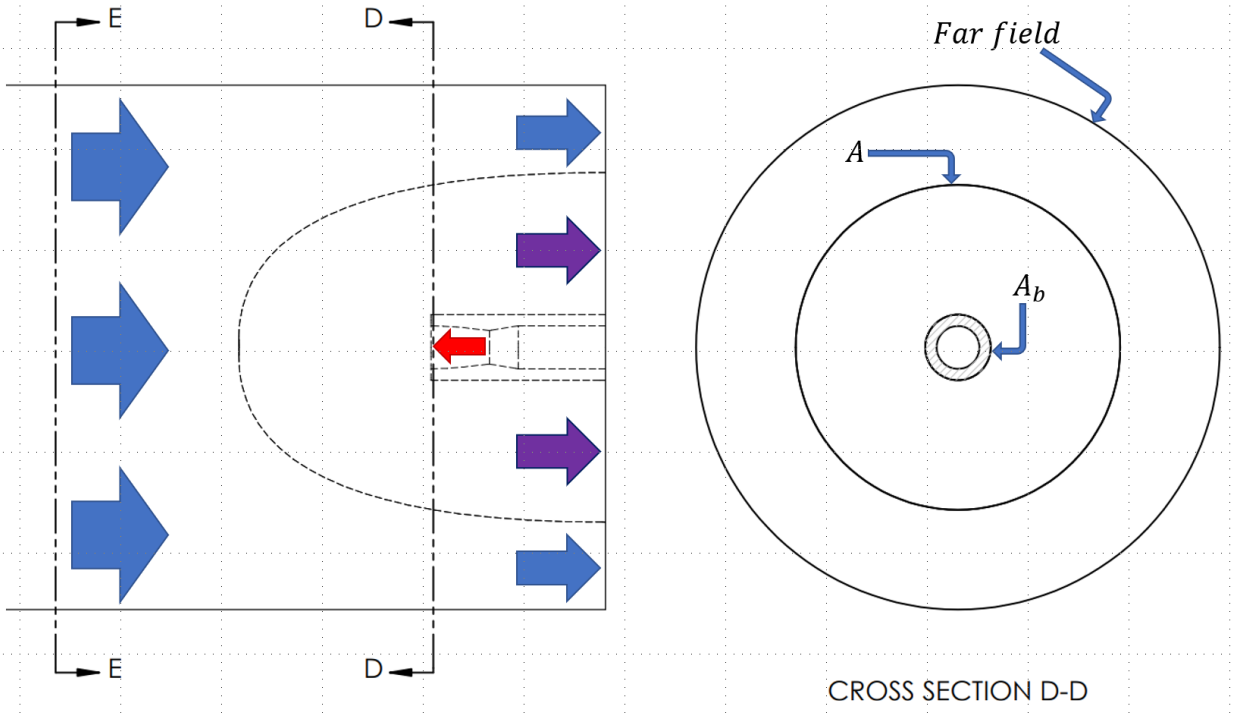

Figure 2.4: CV used for analysis adapted from [3]. Boundaries for the CV include the E-E and D-D cross sections creating a cylindrical CV between the two planes. A streamwise cross sectional view about the central plane is shown on the left with a spanwise cross section at the jet exit plane shown on the right. Blue arrows represent incoming freestream fluid flow and red arrow representing incoming retronozzle flow. Purple represents the mixed region outflow from the CV.

shown in equation 2.11.

$$\frac{A}{A_b} = \frac{U_e}{U_\infty}\frac{P_j}{P_\infty}\frac{A_e}{A_b}\frac{a_\infty^2}{a_j^2}\frac{\gamma_j}{\gamma_\infty} + \int_1^{\frac{A}{A_b}} [\frac{\rho_{m\infty}(r) + \rho_{mj}(r)}{\rho_\infty}]\frac{U_m(r)}{U_\infty} d(\frac{A}{A_b}) \tag{2.12}$$

Further combining and expanding the remaining speed of sound ratio introduces a Mach number ratio and raises the ratio of the ratio of specific heats term to the 1/2 power.

$$\frac{A}{A_b} = \frac{M_e}{M_\infty}\frac{P_j}{P_\infty}\frac{A_e}{A_b}\sqrt{\frac{T_\infty R_\infty}{T_j R_j}}\sqrt{\frac{\gamma_j}{\gamma_\infty}} + \int_1^{\frac{A}{A_b}} [\frac{\rho_{m\infty}(r) + \rho_{mj}(r)}{\rho_\infty}]\frac{U_m(r)}{U_\infty} d(\frac{A}{A_b}) \tag{2.13}$$

Using iscentropic relations, temperature terms inside the square root can be converted to their total temperature counterparts. Additionally, the respective gas constants can be converted to molecular weights of the freestream and retrojet gasses resulting in the final equation shown in 2.13.

$$\frac{A}{A_b} = \frac{M_e}{M_\infty}\frac{A_e}{A_b}\frac{P_j}{P_\infty}\sqrt{\frac{T_\infty}{T_{0,\infty}}}\sqrt{\frac{T_{0,j}}{T_j}}\sqrt{\frac{MW_j T_{0,\infty}}{MW_\infty T_{0,j}}}\sqrt{\frac{\gamma_j}{\gamma_\infty}} + \int_1^{\frac{A}{A_b}} [\frac{\rho_{m\infty}(r) + \rho_{mj}(r)}{\rho_\infty}]\frac{U_m(r)}{U_\infty} d(\frac{A}{A_b}) \tag{2.14}$$

This equation gives rise to two thermodynamically dependant variables defined below:

$$1/\Psi = \frac{MW_j T_{0,\infty}}{MW_\infty T_{0,j}} \quad \text{and} \quad 1/\Gamma = \frac{\gamma_j}{\gamma_\infty}$$

It is hypothesized that by multiplying mass flow rate rate by the inverse of these two variables, the relationship between the normalized interference region and mass flow rate should collapse to a single curve independent of gas composition or temperature, assuming the integrated term does not have a significant influence on the proposed scaling. By further assuming shock shape to be self-similar, taking the square root of this term would equal the normalized shock standoff distance (H/D_b).

In their paper, Korzun and Cassel also attempt a momentum balance to derive a relationship between C_T and the interference region. This derivation will not be repeated here as it does not produce any additional insight beyond what has already been presented. The

most important comment to make is on their definitions regarding C_T. As discussed in the previous section describing the historical scaling parameters used for SRP flow, there is some debate as to which terms can be neglected in a momentum balance introducing variations in the definition of C_T where some researchers neglect ambient pressure contributions to thrust and other do not. In the momentum balance provided by Korzun and Cassel, the C_T referenced earlier in their paper does not appear. Rather they use a term that neglects pressure completely (denoted as C_{T_V}) which they later define as both equal to 1/2 the momentum ratio of the freestream and the jet, as well as the normalized jet thrust assuming only p_∞ equals zero. These two values are not mathematically equivalent. In this thesis the standard definition of C_T defined in equation 2.7 for analysis of shock standoff distances that includes the ambient pressure will be employed given the ambiguity in the literature.

The Finley CV is a more complex beast requiring explanation as to the implicit assumptions made prior to showing the mathematical steps taken to reach his conclusions. The interference region streamline shape was assumed to be that of a spherically blunted cone with semi-angle α as shown in Figure 2.5. This cone represented the leading edge of the CV and continues towards the nozzle until it intersects with the exit plane of the retronozzle. Structures within this region include the recirculation zones, jet shock structures, and shear layers. Finley's notation also uses $p_{0,f}$ to represent the post shock stagnation pressure which will subsequently be updated to modern notation $p_{0,2}$. Additionally, Finley estimated the pressure along the interference region using modified Newtonian theory shown in equation 2.15.

$$p/p_{0,2} = sin^2(\theta) + (p_\infty/p_{0,2})cos^2(\theta) \tag{2.15}$$

The momentum balance Finley presents from this CV is shown in equation 2.15. Finley's approach assumed that, due to the recirculation regions surrounding the retrojet structure, the only locations where momentum exited the CV was in the shear layer (subscript l) and assumed the momentum of this flow is equal to the jet momentum (subscript j), expanded iscentropically and uniformly [4]. Additionally, it was assumed that the dead air pressure p_d could be calculated using equation 2.14 and setting θ equal to α.

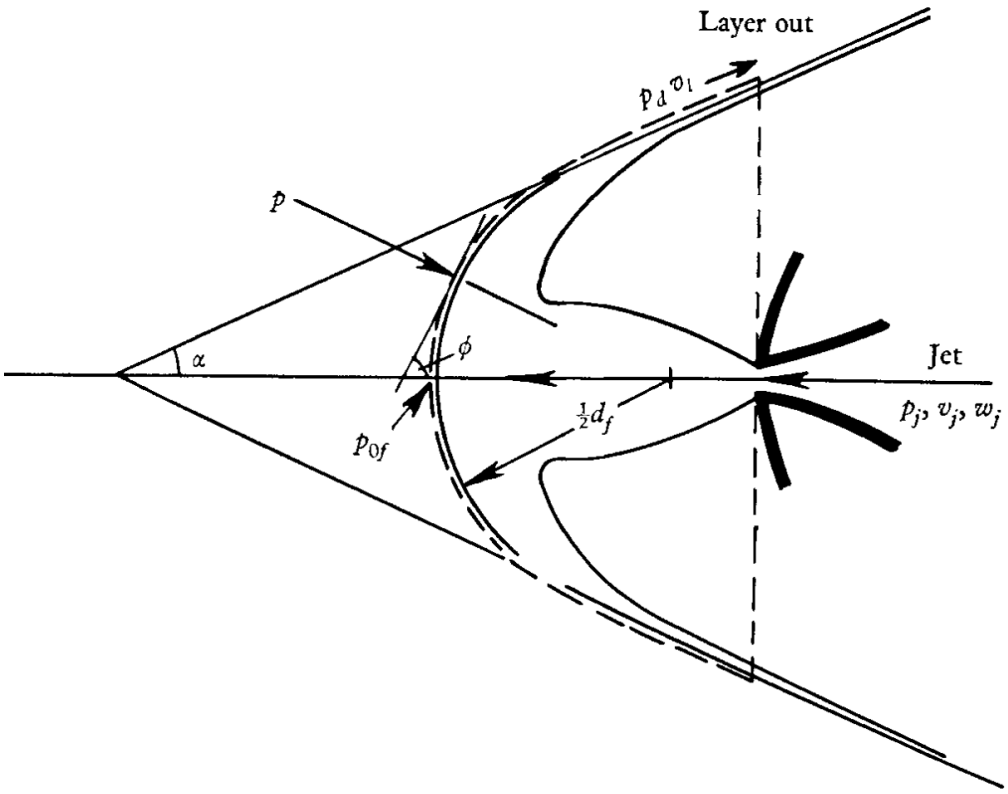

Figure 2.5: Alternate CV adapted from Finley (1966) [4]. Dotted line represents CV with momentum and pressure terms shown with respect to their locations. Bold lines represent nozzle geometry while curved lines represent recirculation regions surrounding the supersonic jet flow.

$$\frac{1}{8}\pi d_f^2 cos^4(\alpha)(p_{0,2} - p_\infty) - \frac{1}{4}\pi d_e^2(p_j - p_d) = \dot{m}_j U_j + \dot{m}_l U_l cos(\alpha) \tag{2.16}$$

The final equation Finley arrived at is shown as 2.16 as an expanded version of equation 2.6 where flowfield parameters equal the ratio of the interface region area normalized by the forebody area.

$$\frac{A_f}{A_b} = C_T(1 + [\frac{U_l}{(C_p T_0)_l^{1/2}}][\frac{(C_p T_0)_j^{1/2}}{p_j A_j + m_j U_j}]cos(\alpha))[0.5[1 - \frac{P_\infty}{P_{0,2}}]cos^4(\alpha)]^{-1} \tag{2.17}$$

While rather complex at first glance, Finley goes on to show that the parameters C_T is multiplied by are purely functions of γ_j, M_e, M_∞,and α [4]. This appears quite promising as it is the first derived equation that could explain the C_T dependence on Mach number observed in the literature.

Unfortunately for the scope of this thesis, the value α cannot be easily found, requiring complex and sensitive experimental construction for velocity field measurements or analytical methods to iterativly find its value. As mentioned in section 2.2, Korzun (2009) [2] attempted to apply Finley's equations to SRP with supersonic jets only to find the results diverged from experimental findings.

Chapter 3

EXPERIMENTAL APPARATUS & METHODS

3.1 Ludwieg Tube

All experiments conducted for this thesis used an open-air test section Mach 2 Ludwieg tube. The tube consists of a 3-inch diameter 10-foot-long pressurized driver section separated from a convergent divergent nozzle by a double diaphragm breech. Downstream of the nozzle assembly is an open air test section in which the retronozzle jet and sting were placed. Two different waveless convergent divergent nozzles were used to attain the Mach 2 freestream flow with area ratios corresponding to $\gamma = 1.4$ (N_2) and 1.28 (CO_2). Schematics for each nozzle are included in Appendix A. Each convergent divergent nozzle has an exit diameter of 2 inches. The contoured Mach 2 nozzles are interchangeable allowing for fast swapping between freestream gasses. Principally, the tube operates by pressurizing the upstream driver section to 124 or 115 psig for the N_2 or CO_2 freestreams respectively. These pressures were chosen to ensure that the freestream flow is perfectly expanded with respect to the atmospheric conditions in the laboratory. The breech is also pressurized to half the fill pressure of the driver section and two 4-mil Mylar diaphragms rated for a 110 psig pressure differential were placed on either end of the breech to maintain its pressure. To trigger the tube, a vent valve is opened allowing the breech to depressurize bursting each diaphragm in sequence (Figure 3.1). This procedure allows for 16 ms of stable freestream flow per test run.

3.2 Nozzle Design

A series of retronozzle geometries were used to conduct the experiments for this thesis shown in Figure 3.2. All nozzle designs are conical with a 4 degree half angle and capable of producing jets with total pressures in excess of 1,300 psi. Four area ratios were chosen to

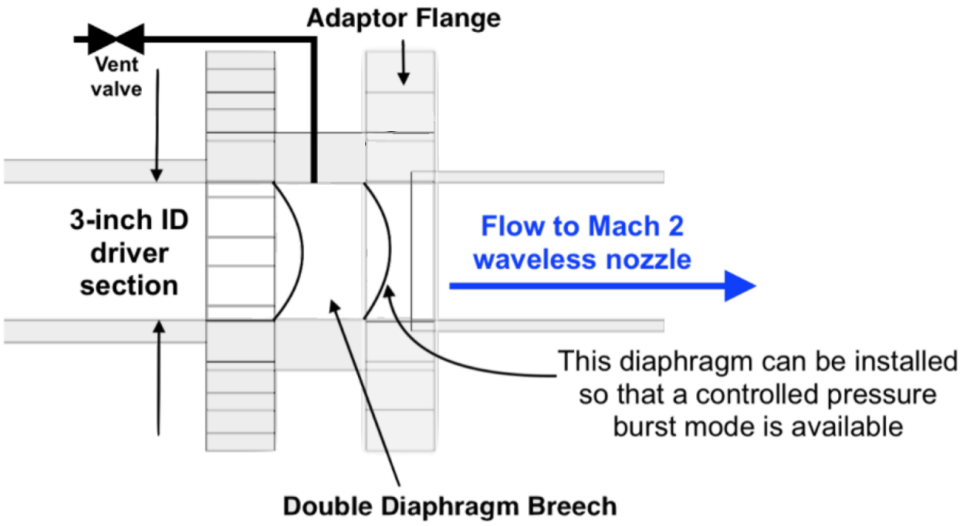

Figure 3.1: Triggering mechanism for Ludwig tube detailed. When triggered, flow in the tube moves from left to right (Adapted from [5]).

produce Mach 2 and 3 retrojet flows for both monotomic and diatomic gasses. Exit diameter was kept constant at 0.082 inches so throat diameter was varied to change area ratio. The retronozzles were machined with an outer diameter of 1/8 of an inch. OML was varied using machined sleeves that fit over the base nozzle allowing for forebody diameters of 1/4 and 3/8 inches to be used while keeping the internal nozzle structure the same. The nozzles were attached to the high pressure gas system using the sting assembly shown in Figure 3.3.

3.3 Schlieren Imaging System

All flow measurements were taken using schlieren photography and recorded at 31,000 FPS using a Phantom v641 camera. Details of the setup are shown in Figure 3.4. A rapidly pulsed LED and printed circuit board designed by Yang (2019) were used as the light source for the schlieren system [5]. The pulse rate of the LED was synced with the frame rate of the high speed camera. As the LED was not on continuously, the current could be massively

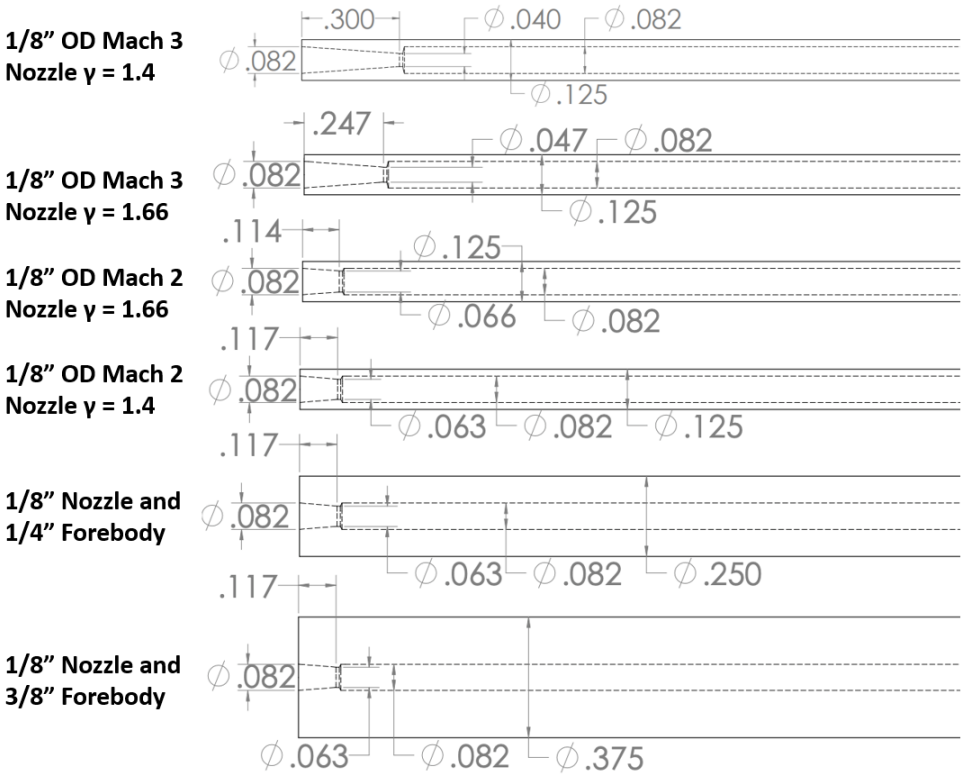

Figure 3.2: Composite of all 6 nozzle variations used in this study (Mach 2 monotomic gas nozzle with 1/4" and 3/8" forebody sleeves not shown).

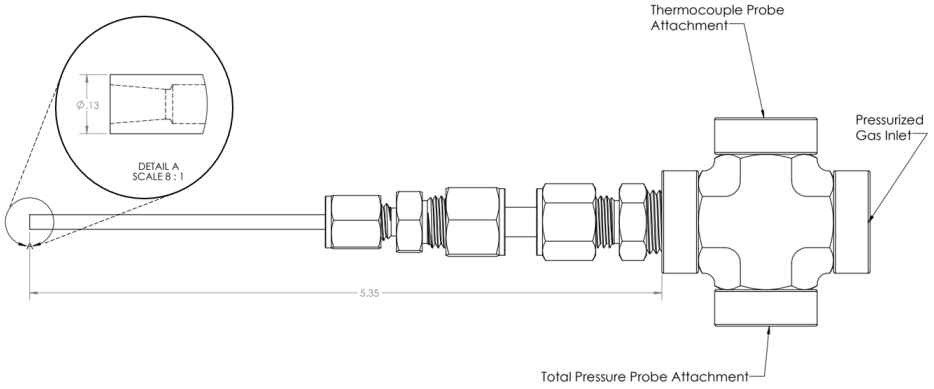

Figure 3.3: Sting assembly for retronozzle with ports for measurement probes identified.

overdrawn to create a brighter image without damaging the LED. Yang (2019) suggests this circuit allows the LED to withstand a peak current of 400 Amps equating to over 20 times its rated value (18 Amps) [5]. Further information on the design of the circuit and light source is available in Yang (2019) and Ho (2019) [5][6].

When illuminated, the light source passes though a condenser lens to focus the beam down to a point approximately 11.5 cm away from the condenser. An aperture is placed at the focal distance of the condenser lens to create a point source of light needed for the schlieren technique to work. A single concave mirror reflects this point source causing the light to pass through the test section twice. This setup is known as a double pass system. Limitations stemming from the physical space within the lab informed the choice of having a divergent beam pass through the test section. The resulting increase in image intensity was noted but did not influence measurements of the bow shock location. Finally, a beam spliter reflects a portion of the incoming light towards the high speed camera for detection. Further details on the schlieren setup can be found in Yang (2019) and Ho (2019).

3.4 Data Processing and Reduction

3.4.1 Shock Standoff Distance

Between 500-600 frames of fully developed SRP flow per test run were captured depending on the test conditions and camera settings. Post-processing of the videos was required once each series of tests were completed for stabilization and analysis purposes. A flow chart summarizing this workflow is shown in Figure 3.5. The retronozzle would move in both the vertical and horizontal directions during each test run due to the impulsive loads from the initial pressure wave exiting the Ludwig tube. This resulted in a drift in the direction of thrust and vertical oscillations primarily attributed to the test article's small diameter and cantilevered position within the test section. Both of these movements were quantified and tracked using post-processing scripts.

A program to find and track the nozzle tip position in each frame was written by Brenton

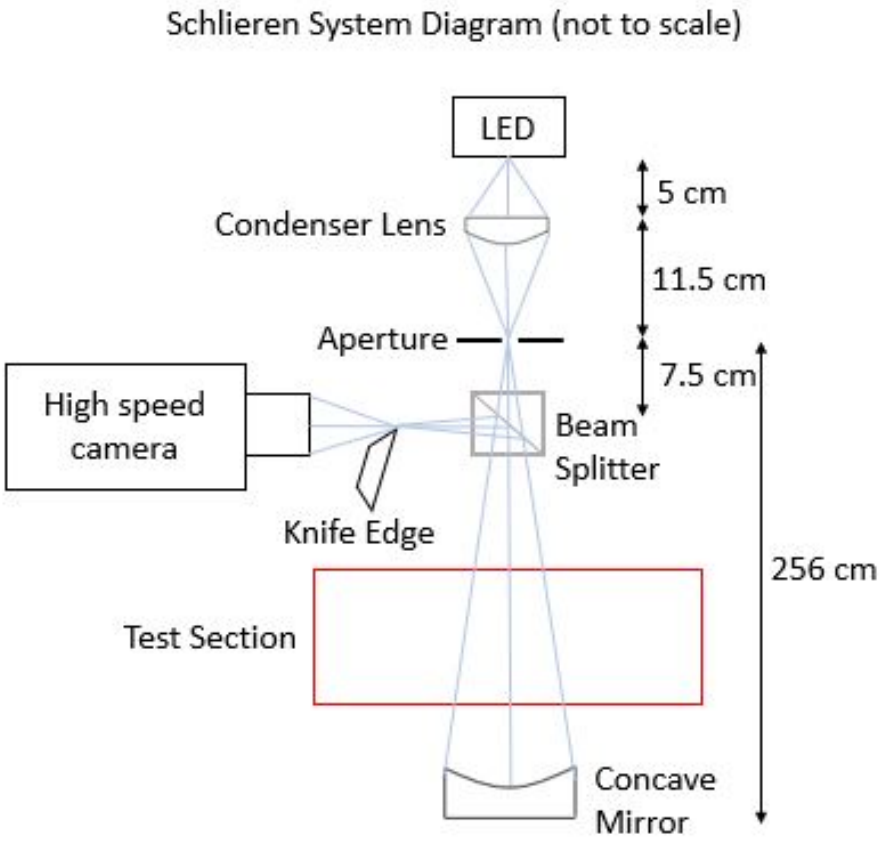

Figure 3.4: Flow visualization diagram adapted from Ho (2019) [6].

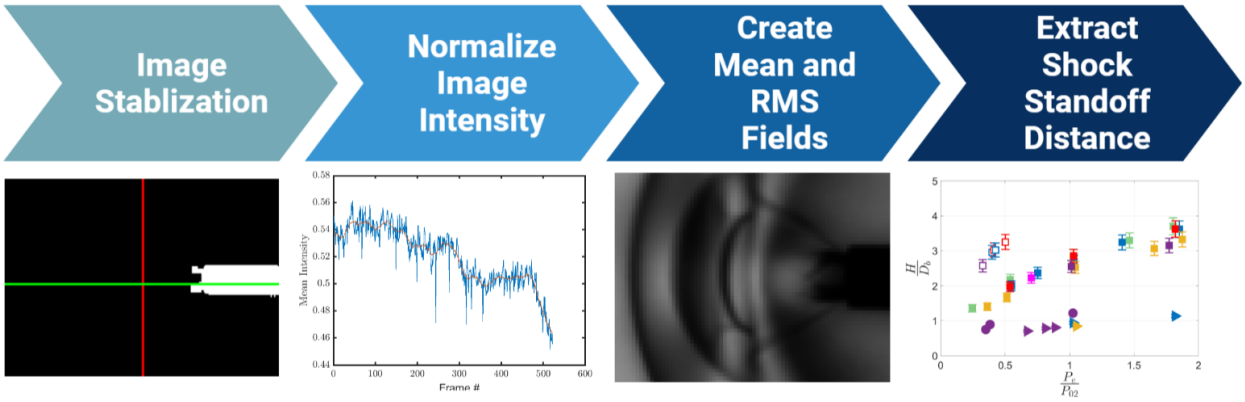

Figure 3.5: Data reduction and image post-processing workflow.

Ho (2019). A K-means clustering algorithm was used to binarize the image into white (nozzle) and black (background) pixels to ease nozzle position tracking. Exact nozzle tip detection was done by interrogating a single row and column of pixels that were found to contain white pixels in every frame of each test run. These vectors of data were checked to have a threshold number of white pixels commensurate with the amount of noise observed in each frame to confirm the presence of the nozzle. Any presence of noise was passed over to improve detection. The average location of white pixels in the column was taken to be the y-location of the nozzle tip. In the row vector, the first white pixel discounting noise was then taken as the x-location of the nozzle. This process was then repeated for each frame in a given test run producing a matrix of stored nozzle tip position data. To further reduce the influence of noise, the location data was smoothed using a linear fit for the x-location and a fourth order polynomial fit for the y-location shown in Figure 3.6 as the orange line [6].

The variation in nozzle position over a given test amounted to an average of a 15 pixel drift opposite to the jet flow in the x direction and an oscillatory motion of ± 4 pixels in the y direction. An example of how this motion affects the quality of the images taken from the camera is shown in Figure 3.7. Tracking the nozzle tip accurately allows for a stabilization program to center each frame about the nozzle tip. See [6] for more information

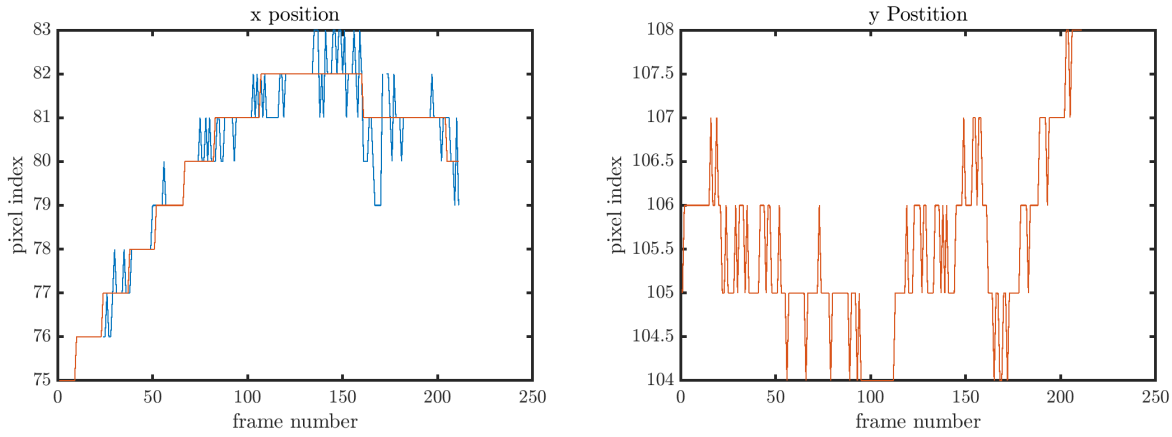

(a) (b)

Figure 3.6: Nozzle tip tracking for CO_2-Ar at $\frac{P_e}{P_{0,2}} = 1.0$.

on algorithms used for image stabilization. Final stabilization accuracy is estimated to be ±1 pixel.

Once the nozzle-centered image series was produced, the frames were normalized by the average image intensity to ensure the RMS fields accurately showed variation in flow motion rather than lighting differences from frame to frame. Equation 3.1 determines the RMS field of a video with n frames of i x j resolution [5].

$$x_{ij,RMS} = \sqrt{\frac{1}{n}\sum_{k=1}^{n}(x_{ijk} - \bar{x}_{ij})^2} = \sqrt{\frac{(x_{ij1} - \bar{x}_{ij})^2 + (x_{ij2} - \bar{x}_{ij})^2 + ... + (x_{ijn} - \bar{x}_{ij})^2}{n}} \quad (3.1)$$

Mean fields were also produced with various levels of zoom to focus on shock and internal SRP plume structure. Equation 3.2 determines the mean field of the same video.

$$\bar{x}_{ij} = \frac{1}{n}\sum_{k=1}^{n} x_{ijk} = \frac{x_{ij1} + x_{ij2} + ... + x_{ijn}}{n} \quad (3.2)$$

A manual process of choosing the nozzle tip location and bow shock location from the mean fields was used to extract shock standoff distances from each test case.

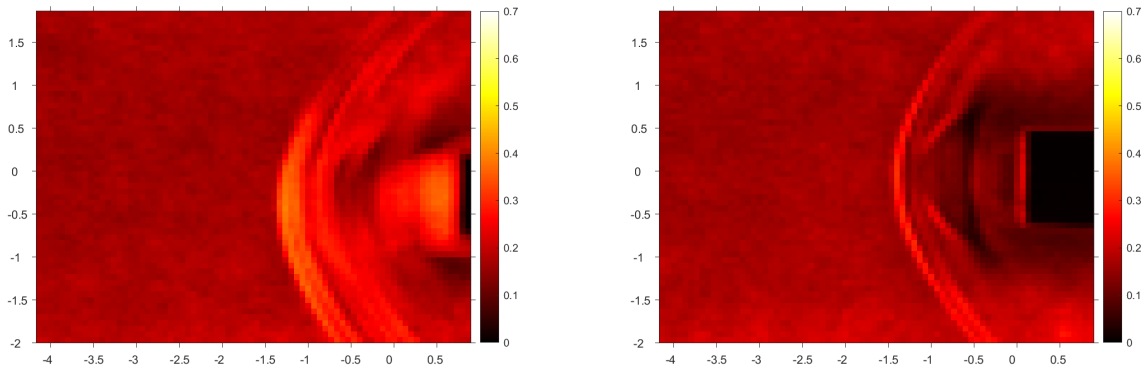

(a) Unstabilized (b) Stabilized

Figure 3.7: Effect of stabilizing nozzle on RMS fields.

3.4.2 Bow Shock Radius Of Curvature

An additional parameter put forward to measure the scaling of the bow shock in the flowfield is the bow shock radius of curvature along the axis of symmetry of the flow. The addition of this parameter can help test if shock shape is independent of standoff distance when varying gas composition. Figure 3.8 shows how exaggerated changes in bow shock curvature can affect the area defined as the interference region used in the CV derivation of the proposed scaling laws without affecting shock standoff distance. If radius of curvature and shock standoff distance are not correlated, the proposed CV will yield inaccurate conclusions.

To extract the radius of curvature (R), the mean field images were binarized using an intensity threshold to highlight regions of high optical density (see Figure 3.9). The gradient of this binarized image was taken to extract the precise pixel location of the leading edge of the bow shock. A fourth order polynomial was fitted to the extracted data points which is shown overlaid on the mean field for comparison in Figure 3.10. The curve is shifted to the

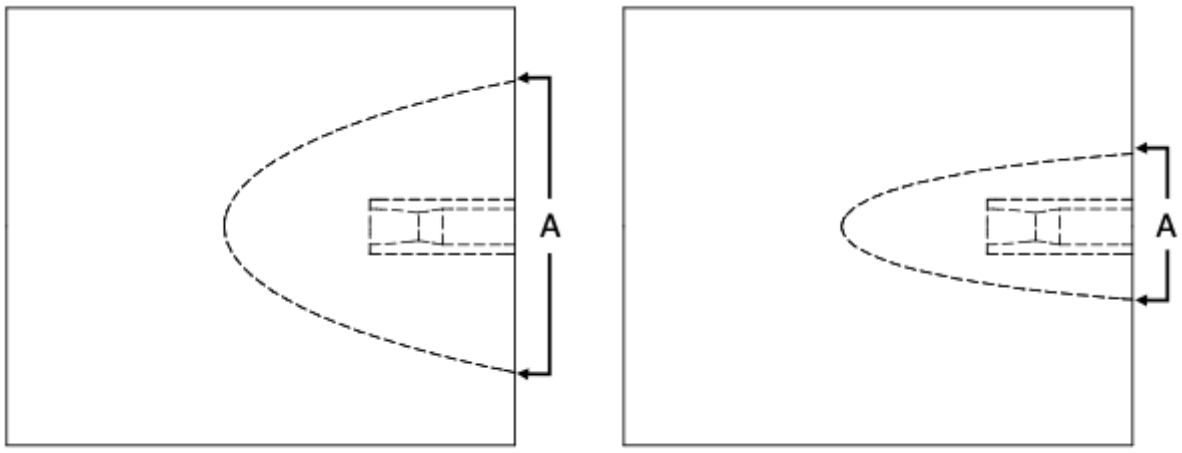

Figure 3.8: Sketch depicting the influence radius of curvature has on the interference region A.

origin and then R is extracted from this curve using the following equation.

$$R = |\frac{1}{d^2y/dx^2}| \tag{3.3}$$

Two separate values become the final products of this analysis R/H and R/D_b. Both values are shown in Figure 3.11 as circles with their respective radii. The first normalized value is used to test the relationship between R and H under different flow conditions. If the bow shock shape is indeed self similar regardless of gas composition, the values of R/H should collapse to a single value. The second term R/D_b is defined as an alternative to H/D_b which is the most common value used to show geometric similarity in SRP literature.

Figure 3.9: Binarized Mean field highlighting regions of high optical density in black. Bow shock location extraction achieved by taking the gradient of this image. (Test conditions: $N_2 - N_2$, $M_e = 3$, $C_T = 4$, $D_b = 1/8$")

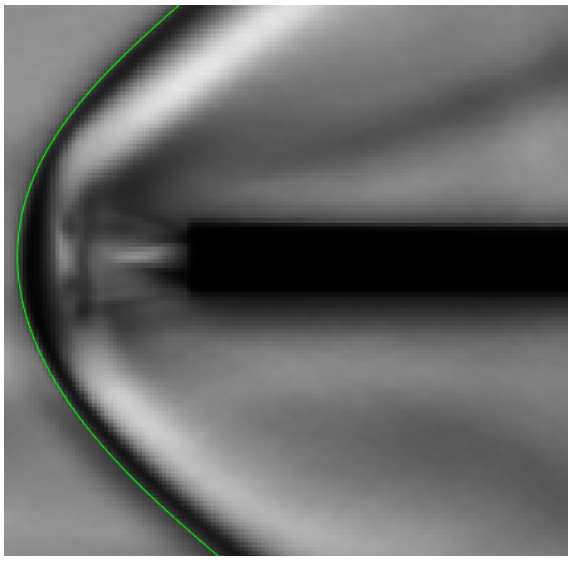

Figure 3.10: Overlay of extracted bow shock shape on top of the mean flowfield. (Test conditions: $N_2 - N_2$, $M_e = 3$, $C_T = 4$, $D_b = 1/8$")

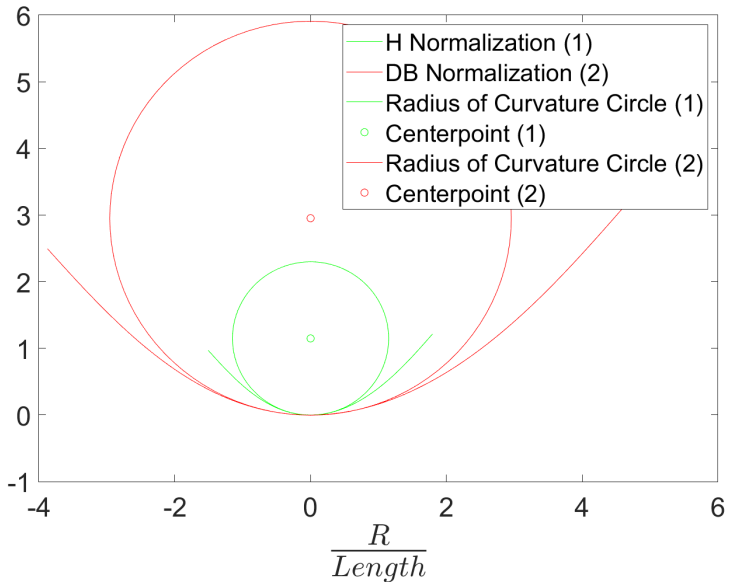

Figure 3.11: Bow shock curves and circles formed by the radius of curvature normalized by both shock standoff distance H (green), and forebody diameter D_b (red).

Chapter 4

DESIGN OF THE RETRONOZZLE GAS PREHEATER AND CONTROL SYSTEM

A key component of this study was the ability to modulate the temperature of the gas species in the SRP flowfield to achieve a significant delta between the retronozzle and freestream gas temperatures to maximize the value of Ψ. The chosen design was a hot pipe whose temperature would be regulated by a resistive heater connected to a control system that the retronozzle gasses would pass through. Convective cooling of the pipe by the internal flow of the retronozzle gas would impart some amount of heat into the gas itself.

4.1 Theoretical Simulation

To better inform the design of the heater system, theoretical models of the heat transfer between the gas and the hot pipe were produced in MATLAB. These models helped to choose appropriate lengths, geometries, and material compositions of the hot pipe as well as the heating element itself. All calculations assumed a He gas flow at 0.0711 kg/s and a pressure of 1200 psi representative of the maximum gas flow for He the experimental setup was capable of. Initial calculations indicated that He gas at this flow-rate and pressure corresponds to the highest heat transfer coefficient of any gas used in these experiments. Using this fact, the He test cases were assumed to cause the largest change in temperature of the hot pipe over a given test period overestimating temperature drop compared to other gas types. The ultimate design goal is to reach a Ψ value of 20 using a heated He retrojet and room temperature carbon dioxide freestream gas flow while minimizing temperature variation of the He during a given test run. This design goal corresponds to a He jet at 200 °C or 473 °K stagnation temperature.

Energy Problem

The energy required to heat He and how quickly that energy can be transferred under the proposed test conditions was calculated to understand the design constraints for heater.

$$\dot{m}tC_p\Delta T = \text{Energy needed to heat gas} \tag{4.1}$$

The C_p value for He at the assumed conditions is 5193 $\frac{J}{kgK}$, the duration of the test is 0.016 sec, and the max temperature of the gas is 505 K.

$$(.48)(.016)(5193)(505 - 293) = 8.46\text{kJ} \tag{4.2}$$

The power supply available for the heater consists of two wall outlets with 120 V 15 Amp AC supplies on separate breakers. This equates to 3600 Watts of available power. Over the course of a single test, assuming perfect energy transfer with no power loss, this equates to

$$0.016 * 3600 = 57\text{J}. \tag{4.3}$$

The energy gap between the required and available energy sources prevent this problem from being treated as steady state. Instead, transient solutions were used with the goal of minimising the temperature change during the short test duration. The ultimate goal would be to have a maximum of 5% temperature variation during a single testing period.

Models

Four different thermal models were investigated for this design study: Lumped Capacitance with Temperature Feedback (LCF), Heat Equation Discritization with Temperature Feedback (PDEF), Lumped Capacitance without Feedback (LC), and Heat Equation Discritization without Feedback (PDE). The latter two models served primarily as references given their extremely conservative assumptions to gauge if the other two were working as expected.

Lumped Capacitance Feedback Model (LCF)

This model relies on the Lumped Capacitance model for heat transfer to calculate the change in temperature of the hot pipe during a test run. The pipe temperature is then used to predict the gas temperature over the length of the pipe at each instant in time. There are a litany of assumptions required to make this model work, but first the mathematics behind lumped capacitance will be discussed.

The lumped capacitance assumption relies on the Biot number

$$Bi = \frac{hL_c}{k_{body}} \tag{4.4}$$

which is a dimensionless constant that describes the ratio between the heat transfer resistances outside a body vs the resistances inside a body [18]. For Bi ≤ 0.1, the lumped capacitance model is generally considered a good assumption [18]. This means that the thermal resistances inside the body are relatively small allowing them to be modeled by simple transient equations.

$$\frac{\Theta}{\Theta_i} = \frac{T - T_\infty}{T_i - T_\infty} = \exp[-\frac{hA_s}{\rho V C_p}t] \tag{4.5}$$

Equation 4.5 describes the non-dimensional temperature change after a specified time t in a given thermal body assuming lumped capacitance [18]. Reformulated, this equation can be written in terms of relevant variables, gas temperature (T_∞) and time t.

$$T(T_\infty, t) = \Theta_i \exp[-\frac{ht}{\rho C_p L_c}] + T_\infty \tag{4.6}$$

All of the variables in Equation 4.6 are functions of the material type the thermal body is made of with L_c being a characteristic length scale of the thermal body. This characteristic length scale for the wall of a pipe is its wall thickness divided by 2, however to keep this model conservative the value used for subsequent calculations was the overall wall thickness [18]. The Biot number calculated for the test conditions is 0.657. This value is greater than 0.1 but by less than an order of magnitude. Nevertheless, the LCF model will be presented

with the caveat that the test conditions are outside the recommended bounds for using the lumped capacitance assumption.

The feedback part of the LCF model references the change in the convective fluid temperature (in this case He) as a result of the heated pipe. As the gas flows through the heated pipe, the gas temperature rises while the tube temperature decreases. This temperature coupling is what makes modeling this heat transfer system so difficult. The gas temperature change is ultimately what we want to quantify from these models. The gas is entering the pipe at a known quantity (assuming total temperature is conserved from the reservoir) and at any given point along the pipe Newton's Law of Cooling/Heating formulated for a constant surface temperature

$$ln(\frac{\Delta T_0}{\Delta T_1}) = -\frac{PX}{\dot{m}C_p}h \tag{4.7}$$

can be solved to find the gas temperature

$$T_{out} = T_s - (T_s - T_{in})exp(-\frac{h\pi DX}{\dot{m}C_p}) \tag{4.8}$$

at that point [18]. The variables in Equation 4.8 are different from those shown in the lumped capacitance equations as now they correspond to the thermophysical properties of the *fluid* rather than the thermal body.

Assumptions made for this model include: a perfectly insulated pipe, negligible radiation heat transfer, a straight pipe, fully developed gas flow, all necessary LC assumptions, slow flow (no pressure drop along the pipe), and ideal gas law using Keye's equations for viscosity.

Heat Equation Feedback Model (PDEF)

When encountering transient heat transfer problems with a Bi number greater than 0.1, the heat equation can be discritized to make predictions with a greater degree of accuracy than a lumped capacitance model [18]. Internal flow through a pipe can be described using the heat equation formulated for a planar wall when the thickness of the pipe is sufficiently small compared to its length [18]. Additionally, boundary conditions corresponding to this heating

problem, convective flow on one side and thermal insulation on the other, can be applied. The solution to this partial differential equation is the infinite series sum

$$\Theta = \sum_{n=1}^{\infty} C_n exp(-\xi_n^2 Fo) cos(\xi_n x) \tag{4.9}$$

where Fo is the Fourier number calculated as

$$Fo = \alpha t / L^2, \tag{4.10}$$

x is the normalized distance from the surface of the plane wall, with 1 representing the inner surface and 0 representing the plane wall, ξ_n are the eigenvalues of the transcendental equation

$$\xi_n tan \xi_n = Bi, \tag{4.11}$$

and finally C_n as coefficients denoted by

$$C_n = \frac{4sin(\xi_n)}{2\xi_n + sin(2\xi_n)} \tag{4.12}$$

The temperature of the pipe over time was calculated by

$$T = (T_{max} - T_\infty)\Theta + T_\infty. \tag{4.13}$$

To calculate the the gas temperature gradient using this model, the same approach for the LCF model was used. Newton's law of heating would take in the pipe temperature and output gas temperature as a function of pipe length. Notably, when finding the pipe temperature at each instant of time using equation 4.13, T_∞ was represented by the average temperature of the gas within each length discritization. Further information on the discrizations used will be explained in the subsequent section. Additional assumptions made for this model were: the infinite series could be approximated by 725 terms, the pipe temperature did not vary with its length only with its thickness (1-Dimensional heat transfer), a perfectly insulated pipe, negligible radiation heat transfer, a straight pipe, fully developed gas flow, and slow flow (no pressure drop along the pipe).

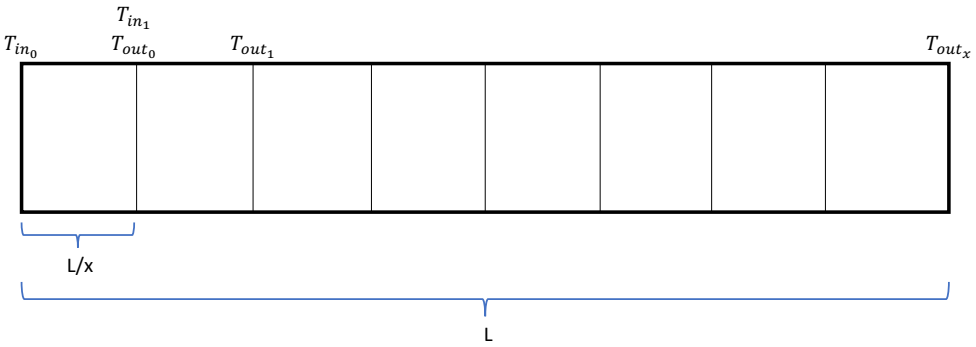

Figure 4.1: Sample discritization of the length of the pipe in which the retronozzle gas would flow. Each inlet and outlet temperatures are calculated using equation 4.8.

Lumped Capacitance and Heat Equation no Feedback

These two models are simply adaptations of the previous two described above. They do away with Newton's law of cooling/heating and instead keep the retrogas temperature at a constant value (293 °K). This is useful as it provides a baseline curve of the hot pipe temperature change as a function of time which is certain to be a conservative estimate.

Code

To simulate the problem in matlab, the pipe through which the gas flows was discritized (Figure 4.1) so the gas temperature over the length of the pipe could be calculated.

To test how different simulation parameters including time and length discirization changed the results from each model, a canonical design was chosen to experiment with these simulation parameters. The design has a length of 12 feet, an inner diameter of 0.37 inches, and an outer diameter of 0.5 inches. Four different length discritization values 5, 10, 40, and 100 were considered and the resulting temperature curves were calculated using the two primary heating models (LCF and PDEF). A 2.1% variation was observed between the 5 and 100 valued versions with corresponding temperature graphs shown in Figure 4.2. These results confirm that the discritization value for length has a relatively small effect on the output of

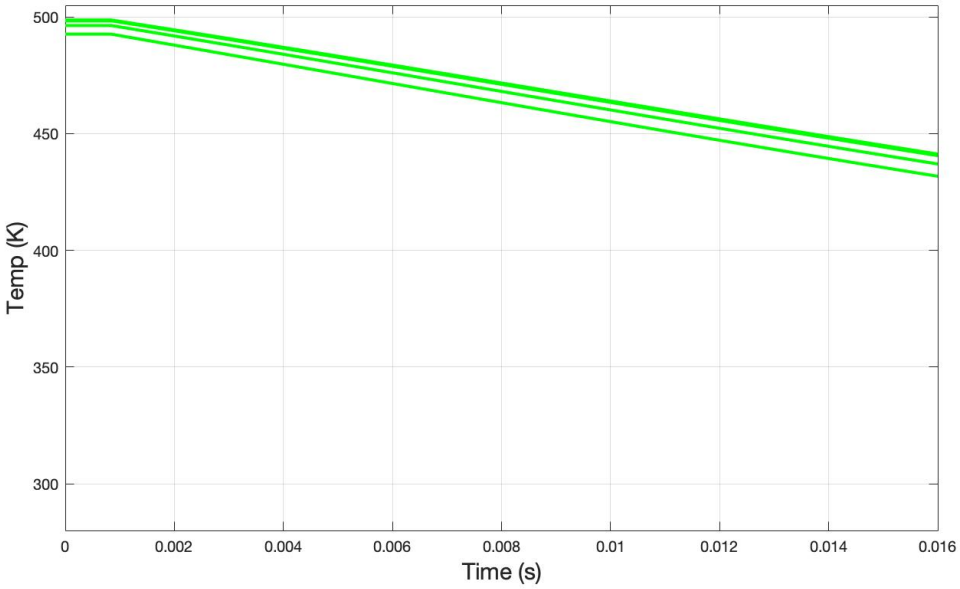

Figure 4.2: Gas temperature curves resulting from four different length discritization inputs 5, 10, 40, and 100 with 5 being the curve shifted closest to the x-axis, and 100 being the furthest. The results come from the canonical design using the LCF model.

the models. Ultimately, 40 was chosen to reduce computation time.

Time discritization was also investigated to understand its effects on the models. Figure 4.3 shows the resulting gas temperature curves using a range of time values for both the LCF and PDEF models. The LCF model is almost entirely independent of the chosen time discritization value with less than 1% variation in model predictions over the 5 cases. The PDEF model curve does change with time step input, however, the most critical difference is that of the variation between the initial and final temperature values along the curve rather than the overall shape of the curve itself. The overall change in temperature variation predicted by each PDEF curve varies by only 2.1% between all five cases. Both models show minimal dependence on time step input. The final value for time discritization resolution was 100. Both length and time discrization values show stable and convergent results.

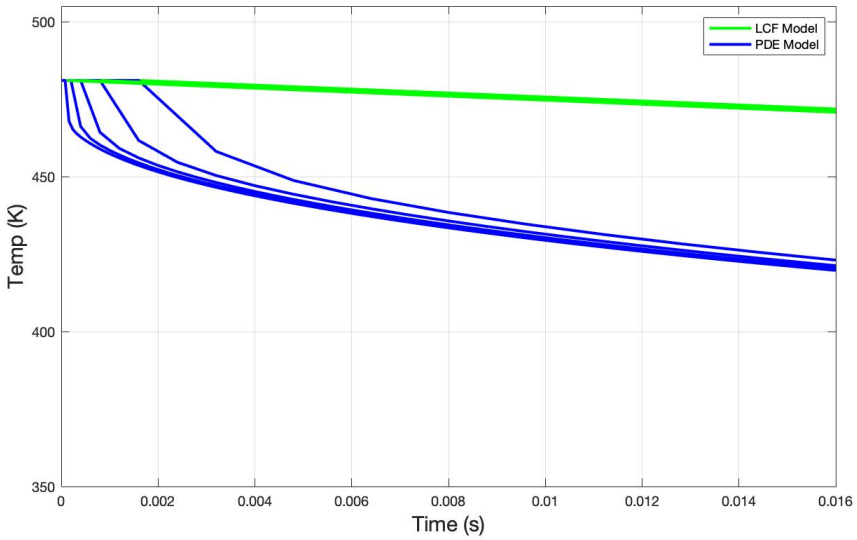

Figure 4.3: Gas temperature curves for both LCF and PDE models using five different time dicsritization values: 10, 20, 40, 100, 250.

All four models of tube temperature variation were plotted using the canonical design inputs in Figure 4.4. As expected, the LC and PDE models predict higher temperature variation than their feedback counterparts. Notably, the LC and LCF models predict much less temperature variation than the PDE and PDEF models. After testing multiple geometric and material configurations using the thermal models, a final configuration was chosen. The geometry for the heater consists of a 12 foot long stainless steel pipe with a 1/2 inch outer diameter and 0.334 inch inner diameter. The length of the pipe was chosen so that the gas flow reached the same temperature as the pipe by the time it reached the retronozzle. Figure 4.5 shows the results of the PDEF model using the final configuration with pipe temperature at the maximum length value (right hand side of the graph) representing the exit temperature of the He gas flow. This geometry combined with the excellent material properties of stainless steel ensure a high structural safety margin and minimal temperature loss over the short duration of a test run.

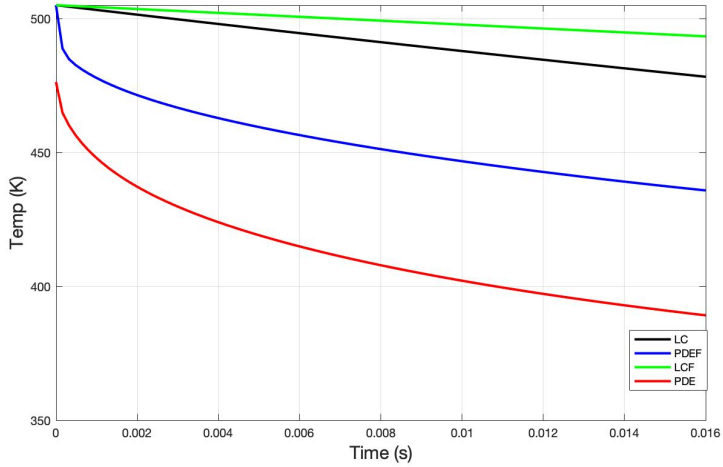

Figure 4.4: Tube temperature curves for all four models

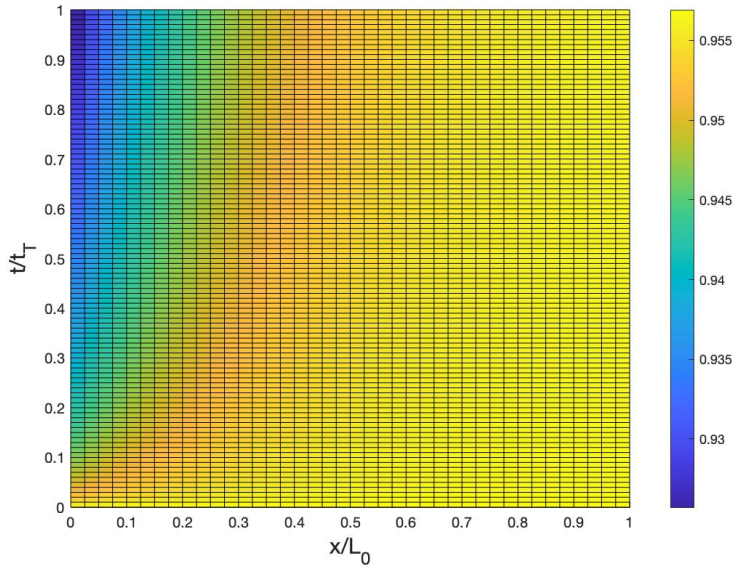

Figure 4.5: Spatiotemporal representation of the hot pipe temperature change using the finalized geometry. The time dimension on the y-axis is normalized by the test duration time (16 ms) with the space dimension normalized by the tube length (12 feet). The color bars show the fractional change in temperature from the original starting value (505 °K).

4.2 Design Overview

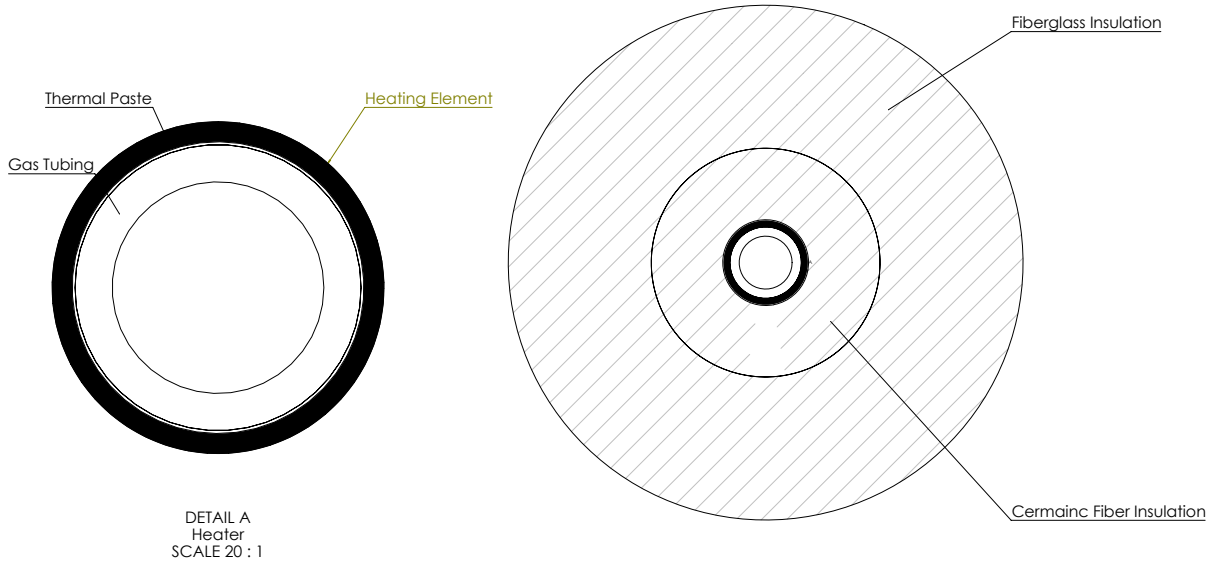

Figure 4.6: Cross sectional view of final heater design.

Other design choices involved the insulation and heating elements for the heater. Three 520 Watt HTS/Amptek flexible resistive heaters wrapped around the outer diameter of the gas supply pipe were chosen as the primary heating elements. They were attached to the hot pipe using a quick drying thermal heat transfer paste. The paste ensures proper contact and adhesion between the surfaces of the pipe and heating elements to maximize the lifespan of the heaters and reduce the chance of a short due to overheating of the resistive wire (Figure 4.6 detail A). The wrapping is secured with fiberglass tape and encased in ceramic fiber insulation clad with foil on one side to minimize radiative heat losses. An final outer layer of fiberglass insulation is then used further mitigating heat losses (Figure 4.6). Three heaters were needed to cover the full length of the pipe. They were connected to a control system that allowed for both On/Off control and voltage control. A veriac was used to modulate the voltage going into the heating elements and an OMEGA CN32PT controller allowed for

precise temperature selection. Tests were conducted with the veriac set to 60% equating to 72 Volts. The controller was set to On/Off control with a set value of 200 °C. This equated to a relatively constant He gas temperature of 170 °C. A full wiring schematic of the control system is shown in Figure 4.7.

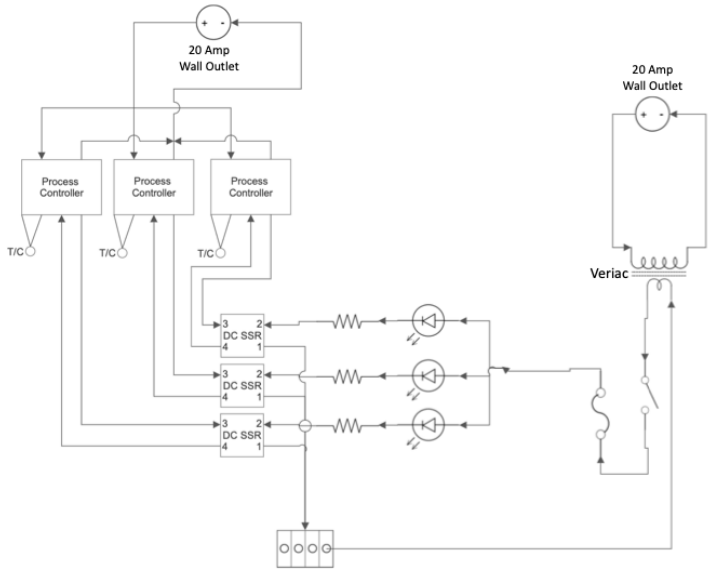

Figure 4.7: Wiring schematic of control system. Controllers and SSRS were grouped into sets of three with each corresponding to a single heater. LEDs were wired into the circuit to give the operator a visual indication of which heaters were on at any given time.

Chapter 5

RESULTS AND DISCUSSION

5.1 Test Conditions and Parameter Space

Given the number of potential variables being investigated for this study, a structure was needed to organize the experiments. Tests were carried out in three separate groups. Each group matched either $P_e/P_{0,2}$, C_T, or $\dot{m}_j/\dot{m}_\infty$ while varying D_b, M_e, Ψ, and Γ. All tests focused on the steady high thrust region of SRP flow with a constant M_∞ value of 2. To change M_e, throat area (A^*) was varied keeping the nozzle exit area (A_e) and conical divergence angle (4°) constant across all geometries. A summary of the test conditions investigated and symbols used in subsequent figures are shown in Table 5.1. For a full tabulated list of all test conditions including matched and varied parameters, refer to Appendix B.

Symbol	Freestream-Retro	Condition			
■	$CO_2 - Ar$	$\Gamma = 1.29$	$\Psi = 1.15$	$D_b = 0.125$	$M_e = 2$
■	$CO_2 - He$	$\Gamma = 1.29$	$\Psi = 11.43$	$D_b = 0.125$	$M_e = 2$
■	$CO_2 - He$	$\Gamma = 1.29$	$\Psi = 16.3 - 17.1$	$D_b = 0.125$	$M_e = 2$
▶	$CO_2 - He$	$\Gamma = 1.29$	$\Psi = 11.43$	$D_b = 0.375$	$M_e = 2$
□	$CO_2 - He$	$\Gamma = 1.29$	$\Psi = 11.43$	$D_b = 0.125$	$M_e = 3$
□	$CO_2 - He$	$\Gamma = 1.29$	$\Psi = 16.3 - 17.1$	$D_b = 0.125$	$M_e = 3$
■	$CO_2 - N_2$	$\Gamma = 1.09$	$\Psi = 1.58$	$D_b = 0.125$	$M_e = 2$
▶	$CO_2 - N$	$\Gamma = 1.09$	$\Psi = 1.58$	$D_b = 0.375$	$M_e = 2$
■	$N - He$	$\Gamma = 1.19$	$\Psi = 7.40$	$D_b = 0.125$	$M_e = 2$
■	$N_2 - N_2$	$\Gamma = 1.0$	$\Psi = 1.06$	$D_b = 0.125$	$M_e = 2$
□	$N_2 - N_2$	$\Gamma = 1.0$	$\Psi = 1.06$	$D_b = 0.125$	$M_e = 3$
●	$N_2 - N_2$	$\Gamma = 1.0$	$\Psi = 1.06$	$D_b = 0.25$	$M_e = 2$
▶	$N - N$	$\Gamma = 1.0$	$\Psi = 1.06$	$D_b = 0.375$	$M_e = 2$

Table 5.1: Figure legend and test conditions.

Limitations based on the testing apparatus or stability conditions made it so that not every matched case could be repeated with every possible gas and geometry condition. An example is the $D_b = 1/8$" geometry at $P_e/P_{0,2}$ values of 0.3 was steady whereas the $D_b = 3/8$" geometry under the same conditions was not. Similarly, for cases where $M_e = 3$ it was impossible to reach $P_e/P_{0,2}$ greater than 0.6 given the pressure limitations of the experimental apparatus.

Other constraints can be gleaned from Figure 5.1. As forebody diameter increases (see Table 5.1 for legend key), gains in both C_T and mass flow rate ratio diminish for a given increase in pressure. This relationship explains why high C_T and mass flow rate ratio data is absent from this dataset. A similar but inverted relationship occurs when looking at

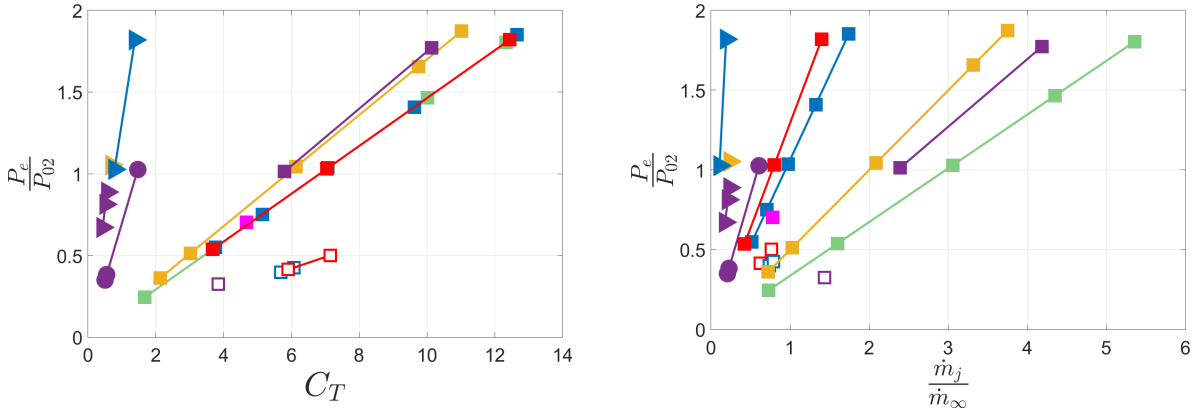

(a) (b)

Figure 5.1: Parameter space of test conditions highlighting relationships between pressure ratio and C_T and mass flow rate ratio.

M_e. Small increases in pressure ratio for the $M_e = 3$ data yields much higher gains in C_T than for Mach 2. Changes in gas combination, which translate to variations in Γ, did not impose similar constraints, which can be seen from the slight changes in slope for the central group of lines in Figure 5.1a. The mass flow rate relationships presented in Figure 5.1b highlight a dependence on Ψ which is not present in the C_T results. The slope for each test condition increases with Ψ given the same forebody and M_e values. This result hints that the hypothesis regarding a collapse of the mass flow rate ratio data with Ψ may be correct.

5.2 Experimental Results

5.2.1 Mean and RMS Images

Mosaic images of the mean and RMS fields extracted from the data analysis workflow described in section 3.4.1 are shown below in Figure 5.2 and Figure 5.3 respectively. These fields represent zoomed-in images where the primary SRP shock structure can be seen. Nozzle tip position across all images is kept constant so the movement of the bow shock and plume

structure can be more easily observed. Twelve cases are presented where the columns of the mosaics represent the pressure ratio of each test and the rows represent the gas conditions varied across each experiment. In this selection of images only Ψ and Γ were varied across each chosen pressure ratio keeping M_e and D_b constant.

The mean image mosaic in Figure 5.2 is structured in such a way that pressure ratio ($P_e/P_{0,2}$) increases from left to right, and Ψ increases from top to bottom. The nozzle position within each frame is kept constant so direct visual comparisons of the shock structures and their scales is possible. It is clear that increasing $P_e/P_{0,2}$ across the range between 0.5 - 1.75 also increases the shock standoff distance (H). Additionally, Figure 5.3 shows very little movement in the region of the bow shock for all presented conditions, indicating that all cases shown are steady. This result directly contradicts findings presented in Korzun and Cassel (2020) where it is postulated that for flow to be self-similar, $P_e/P_{0,2}$ must be greater than unity [3]. Their reasoning is that when $P_e/P_{0,2}$ is above this threshold the retrojet structure is under-expanded and becomes steady [3]. Further discussion regarding the expansion conditions and the influence D_b has on stability will be included in subsequent sections.

The influence, or lack-thereof, that Ψ and Γ have on the matched pressure ratio conditions can be evaluated by observing the bow shock locations in Figures 5.2 and 5.3. Looking from top to bottom in these mosaics, neither Ψ nor Γ appear to scale H when pressure ratio is matched. The only visual effect these conditions seem to cause is variation in the plume shock structure. Likely causes for this variation include the differences in the refractive index of the gasses, He having a lower index of refraction than the other gasses used. Additional effects include the influence of Γ on the wave speed and angles present in the plume structures.

Similar images from the matched mass flow rate ratio cases are included in Figure 5.4. These cases varied all the same parameters as the matched pressure ratio cases with additional Ψ values included as well as increased M_e values. Again, all presented cases are representative of steady flow indicated by the RMS images. The cases are presented in order of smallest to largest H value. A clear trend between Ψ and H can be seen in these images

where higher values of Ψ increase H. Additionally, the variation of M_e indicates that jet exit Mach number also increases the shock standoff distance suggesting that any proposed scaling law will depend on M_e in addition to Ψ. There also seems to be a relationship between the Mach disk curvature and M_e. This can be seen by comparing the different jet exit Mach values for $CO_2 - He$ cases of equal Ψ values. Cases where $M_e = 3$ display a more blunted Mach Disk when compared to the same conditions at $M_e = 2$. The influence of this Mach Disk curvature on the actual bow shock shape is not clear.

5.2.2 Radius Of Curvature

As described in section 3.4, two primary metrics for evaluating flowfield similarity were extracted from each test case; shock standoff distance (H), and the radius of curvature at the tip of the bow shock (R). The scaling law derivation from Chapter 2 relates thrust coefficient and scaled mass flow rate ratio to the disturbance area caused by the SRP interaction (A). Therefore, R is assumed to be directly proportional to the shock standoff distance H such that H can directly stand-in for the square root of A. As such, normalizing the extracted shock profiles by H for each test case at a M_e value of 2 (Figure 5.5) shows the shock profiles collapse within a narrow band, which helps validate this assumption. However, the exit Mach 3 cases (unfilled symbols) are more tightly concentrated than the rest of the dataset by a small degree indicating a possible dependence on M_e.

Figure 5.6 shows how R/H is broadly insensitive to flowfield parameters. Average values for R/H across all conditions approach 1.3. There is however a noticeable spread within the data that we believe can be attributed to the R measurements themselves being vulnerable to bias introduced from the experimental setup. Potential sources of bias in the presented data include recoil from the impulsive freestream blast influencing retronozzle angle of attack as well as oscillations in the retronozzle induced by the freestream flow which have been shown to occur in previous sections. The mean value for $M_e = 3$ cases seems to be concentrated slightly offset from the mean location of the Mach 2 cases, but given the overlap of other datapoints this distinction is not certain.

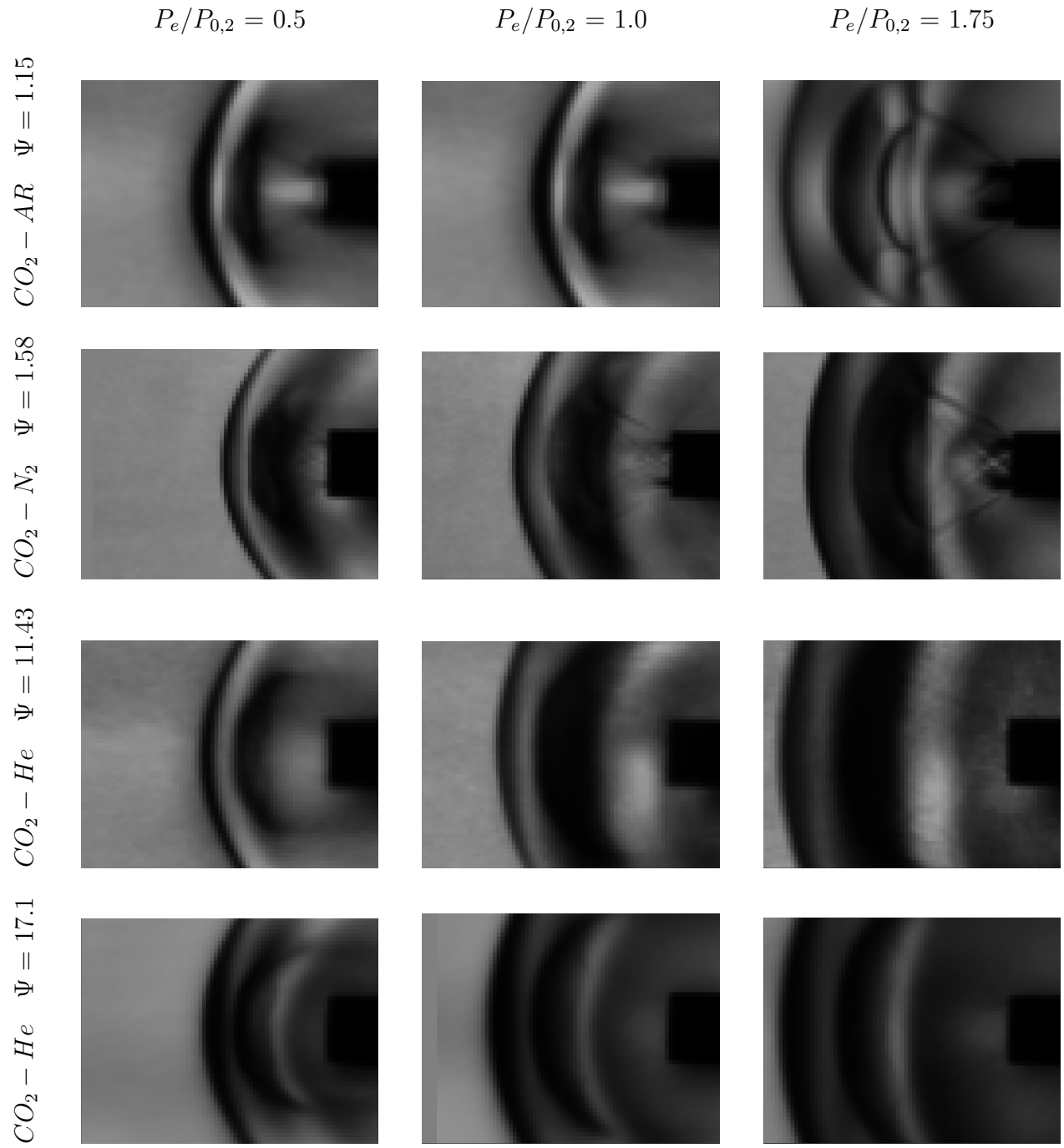

Figure 5.2: The Mean image of SRP flowfields for all matched $P_e/P_{0,2}$ cases for the D_b = 1/8" geometry.

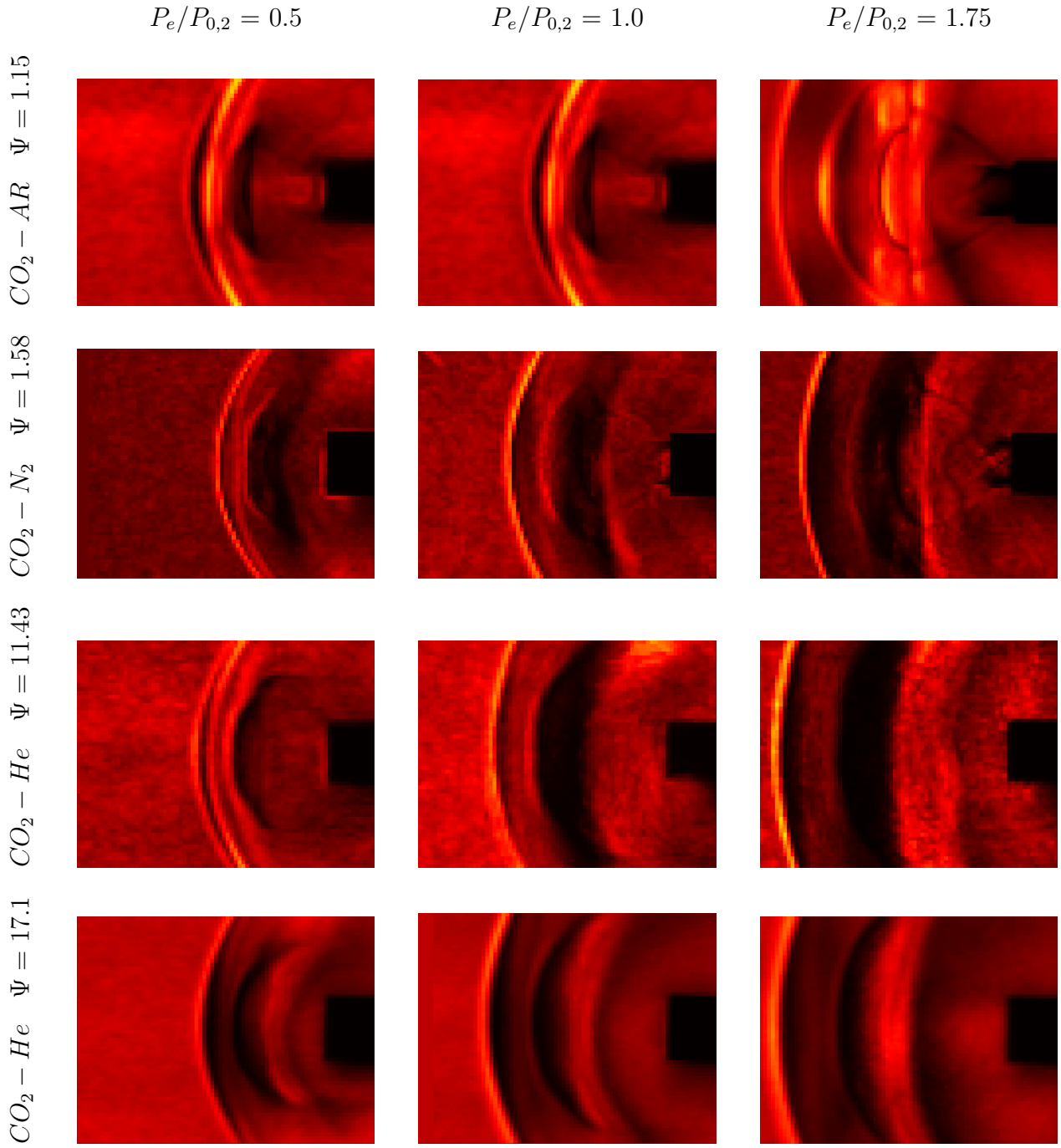

Figure 5.3: The RMS image of SRP flowfields for all matched $P_e/P_{0,2}$ cases for the D_b = 1/8" geometry.

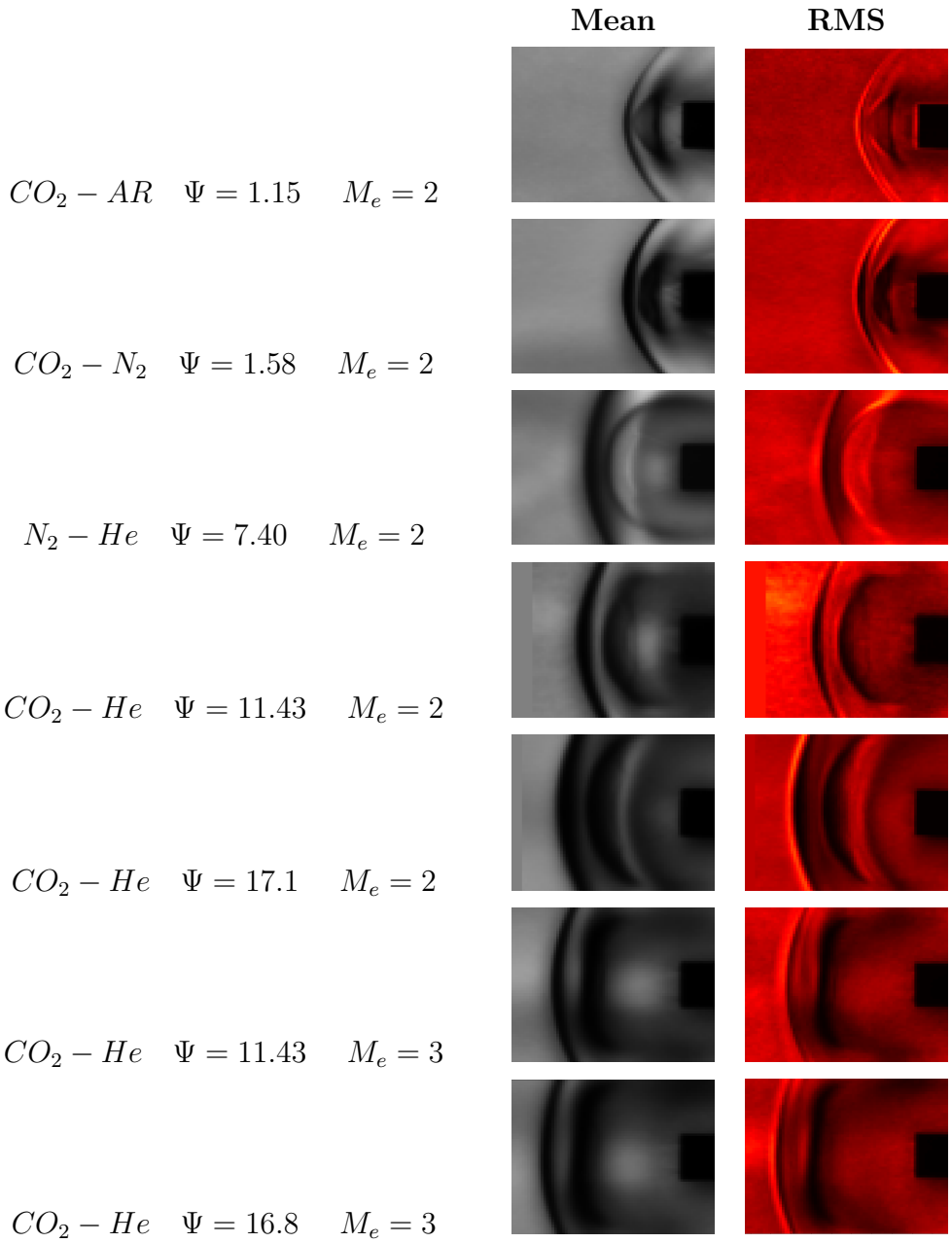

Figure 5.4: Mean and RMS images of the SRP flowfield using 1/8" nozzle diameter comparison at $\frac{\dot{m}_j}{\dot{m}_\infty} = 0.75$.

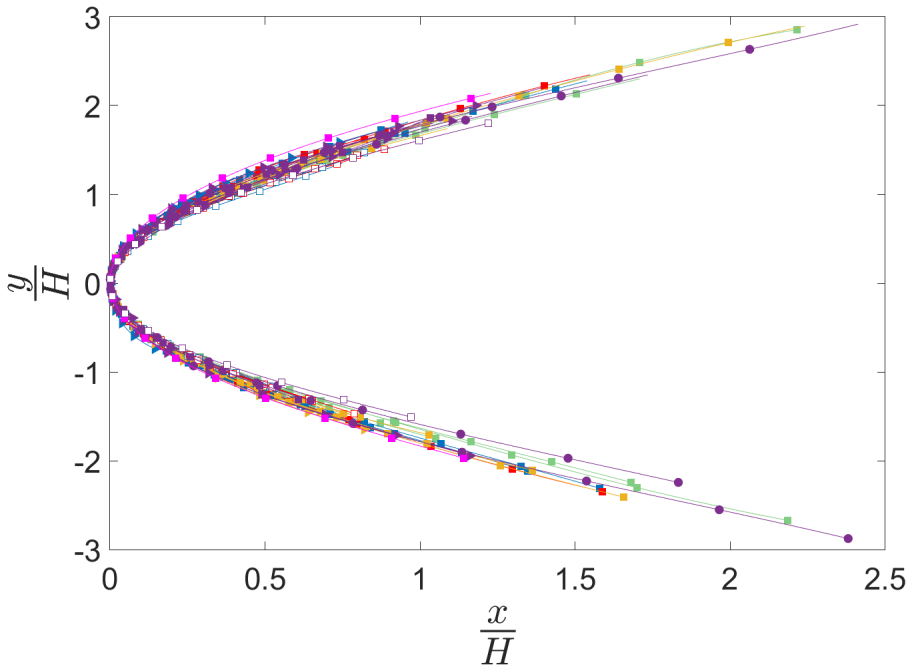

Figure 5.5: Extracted shock curves for all presented cases. Colors and marker shapes correspond to Table 5.1. Curves represent best fit lines for each shock using a fourth order polynomial.

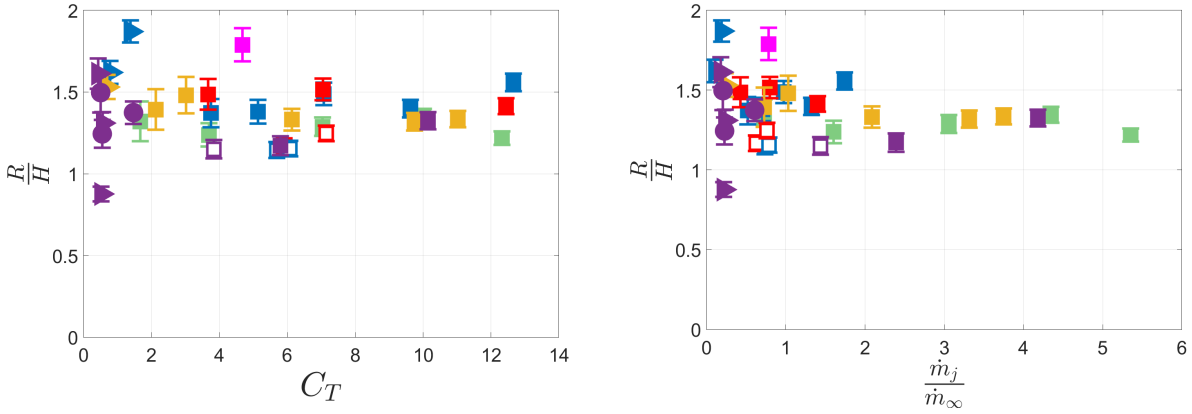

Figure 5.6: Relationship between R/H vs mass flow rate ratio and C_T. Trend shows R/H remains constant around 1.3 regardless of increases in either flow parameter.

5.2.3 Nozzle Exit to Post-Shock Stagnation Pressure Ratio ($P_e/P_{0,2}$)

The term $P_e/P_{0,2}$ serves as an approximate reference for the expansion conditions of the retronozzle jet [3, 7]. This term is more useful than simply using a total pressure ratio as the post shock stagnation pressure ratio is the most easily calculated proxy for the base pressure on the retronozzle body [3, 7]. As shown in Figure 5.7, observing consistent trends when examining how shock standoff distance scales with increases in pressure ratio is difficult as many of the investigated parameters listed in previous sections have an unknown effect on shock standoff distance and radius of curvature. Most obvious are the effects from M_e, seen to increase shock standoff distance for a given pressure ratio, as well as forebody-to-nozzle exit diameter ratio (D_b/D_e), seen to decrease the shock standoff distance. What is not obvious from this plot are the effects that the chosen thermodynamic parameters have on shock standoff distance. No clear trend emerges relating Ψ and Γ, or a combination of the two, with shock standoff distance.

Important to note is that while the post shock stagnation pressure ratio graphs shed

little information as to potential thermodynamic scaling laws, when comparing Figure 5.7a with 5.7b, the trends in the data look strikingly similar. Further explanation as to the significance of this trend with be provided in later sections, but this observation is a key piece of evidence in validating the use of radius of curvature as a geometric length scale that should be explored in addition to shock standoff distance.

Previous studies have supported the theory that for SRP flowfields to be self similar they must be highly under-expanded[1, 4, 14], and further define this condition to occur at $P_e/P_{0,2} > 1$ [3]. Expansion conditions are also postulated to predict stability within the flowfield by representing a transition point between flow regimes 2 and 3 (see Figure 2.1 for reference) when the jet becomes highly under-expanded [3]. A wide variety of conditions, both below and above that threshold, were collected for this thesis using various gas combinations, retronozzle geometries, and retrojet Mach numbers. Figure 5.7 provides expanded evidence that contradicts this theory showing that for a simple single nozzle configuration, stable self similar flowfields can be produced with $P_e/P_{0,2}$ values far below unity. While there has yet be to a consensus on the parameters that predict the stability transition point, it is well understood that geometry plays a large role in determining stable flow conditions [3]. Current results suggest that increases in D_b/D_e will also increase the transitional value for $P_e/P_{0,2}$ [8].

5.2.4 Coefficient of Thrust (C_T) and mass flow rate Ratio ($\dot{m}_j/\dot{m}_\infty$)

Shock geometry is shown to be much more dependant on thrust coefficient than pressure ratio. Figure 5.8a shows shock standoff distance follows along a clear curve independent Ψ, Γ, or D_b/D_e for a given M_e value. This is the first time such an observation can be conclusively stated due to the uniqueness of this dataset. There is indications of M_e dependence in figure 5.8a, however, this dependence does not appear in Figure 5.8b which uses radius of curvature as the geometric measurement for the bow shock. This observation is more difficult to say conclusively as a hypothesized sensitivity of the radius of curvature to experimental bias makes the collapsed curve in Figure 5.8b more messy, but would align with the influence M_e

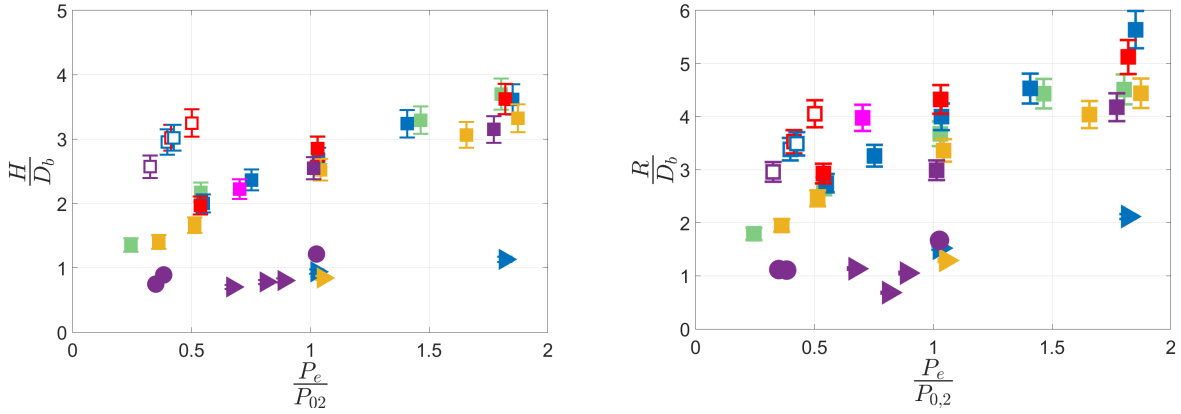

(a) (b)

Figure 5.7: Pressure ratio data for both geometric scaling factors.

has on the collapsed shock shapes in Figure 5.5. A final note comparing the two geometric parameters is that while trends appear similar, the magnitudes of H/D_b and R/D_b are quite different.

Mass flow rate ratio data (Figure 5.9) shows a bifurcation of the data points into regions whose test conditions have values of Ψ on the order of 1, and those of order 10. This separation, that increases with Ψ, shows a clear potential for data collapse. Highlighted in Figure 5.9a is the importance of temperature in the Ψ parameter with heated cases displaying statistically significant increases in H/D_b compared to unheated cases at the same test conditions.

Additionally, mass flow rate ratio results also show trends similar to those seen in the C_T results. When comparing Figures 5.9a and 5.9b, radius of curvature results indicate a possible independence to M_e while shock standoff distance does not display this characteristic. Similar differences in magnitude between H/D_b and R/D_b are also apparent as R/D_b appears to increase more rapidly with respect to mass flow rate ratio than H/D_b.

Across the board, the dependence of shock standoff distance on M_e is consistent with

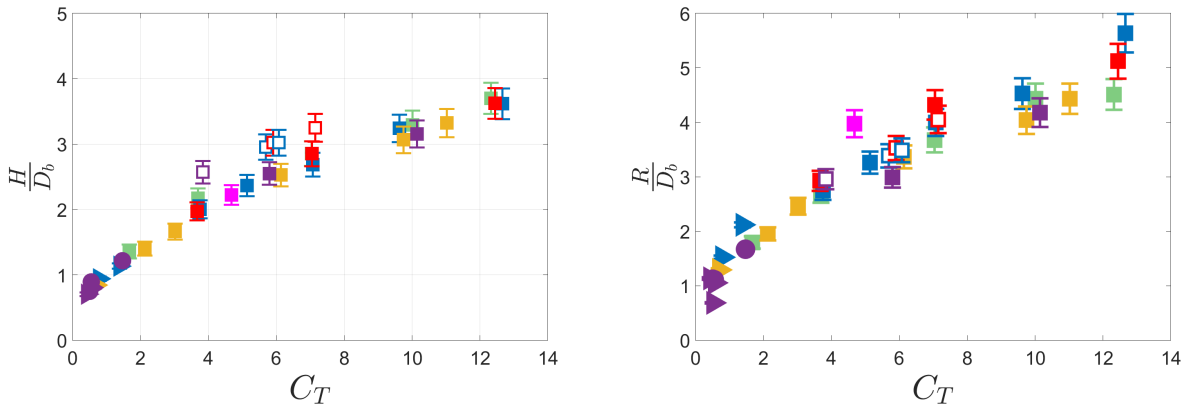

(a) (b)

Figure 5.8: Coefficient of thrust data for both geometric scaling factors.

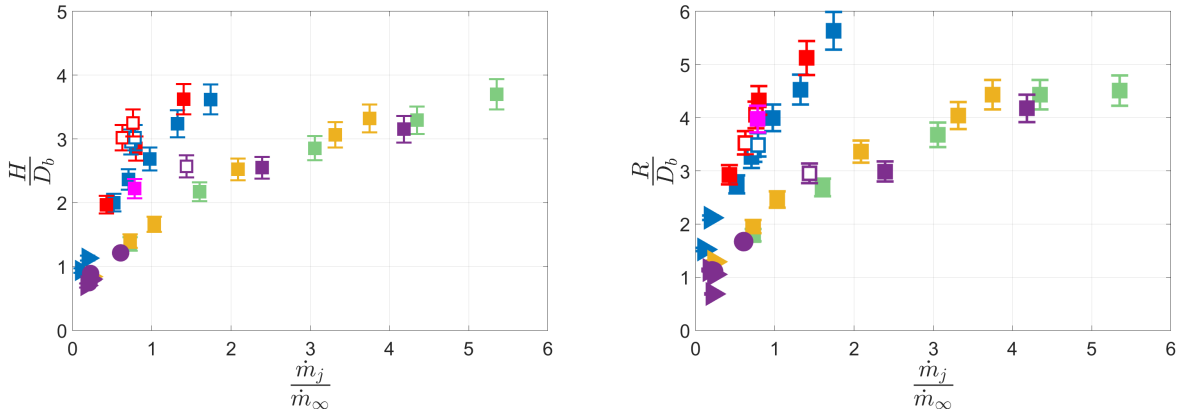

(a) (b)

Figure 5.9: mass flow rate ratio data using both H and R for visualization.

findings from Romeo and Sterret [1] but contradicts recent findings from Gutsche et al [7] who showed almost no jet exit Mach number dependence across their range of conditions which included various freestream mach numbers as well. Scaling factors that account for this Mach number dependence are presented in the next section.

5.2.5 Data Collapse

We have identified two candidate scaling laws one based on C_T and the other on mass flow rate. C_T results will be discussed first. The addition of Mach number ratio (defined as M_e/M_∞) collapses the data to a power curve shown in Figure 5.10a. For convenience, this term will be referred to as the modified thrust coefficient or C_{TM}. Mach number ratio scaling is an empirical result not supported by the derivation shown in section 2.3. Additional observations include that the direct relationship between the square root of C_T, or in this case the square root C_{TM}, and shock standoff distance observed by other researchers holds [3, 4, 7, 14] (Figure 5.10b).

The curve fit that best estimates the relationship between C_{TM} and normalized shock standoff distance is represented by the equation $H/D_b = 1.01\sqrt{C_{TM}} + 0.04$ with an R^2 value of 0.993. Confidence intervals within 95% for this fit are shown as a highlighted blue region in Figure 5.10b. Extrapolation of this line to zero intercepts the y-axis between -0.002 and 0.112 according to the confidence interval.

The second candidate scaling parameter Ξ, which will be referred to as the scaled mass flow rate ratio, arises from an analysis of the raw mass flow rate ratio shock standoff trends. As predicted from the analysis in section 2.3 and the observations made when graphing the test parameter space, the mass flow rate ratio results collapse as a function of Ψ and Γ raised to the one half power (Figure 5.11a). M_e dependence was also observed in the results which the addition of the Mach number ratio term seems to correct for. Like C_{TM}, Ξ raised to the one half power has a linear relationship with shock standoff distance (Figure 5.11b). The curve fit that best represents this relationship is $H/D_b = 1.593\sqrt{\Xi} + 0.025$ with an R^2 value of 0.9918. The region bounded by the 95% confidence interval for both curve fit coefficients

is highlighted in blue.

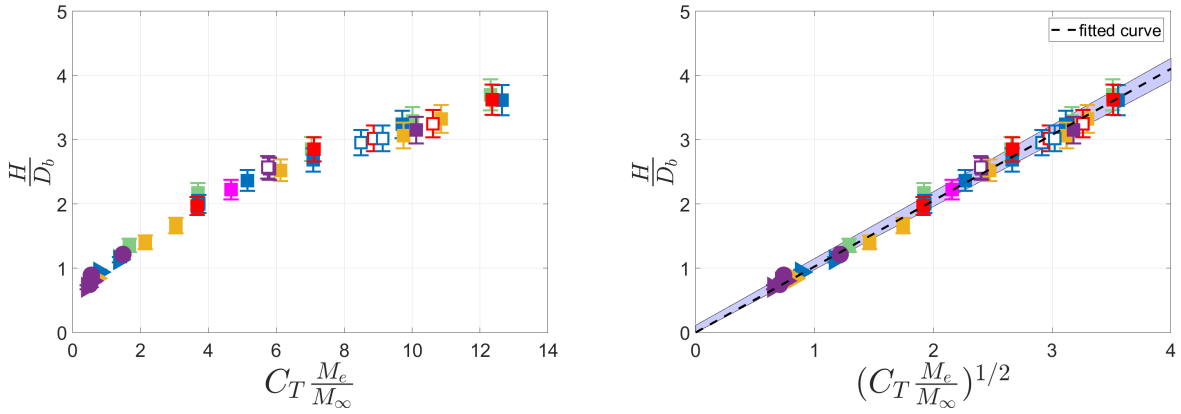

(a) (b)

Figure 5.10: Trends in shock standoff distance for steady flow conditions as functions of both thrust coefficient and pressure ratio.

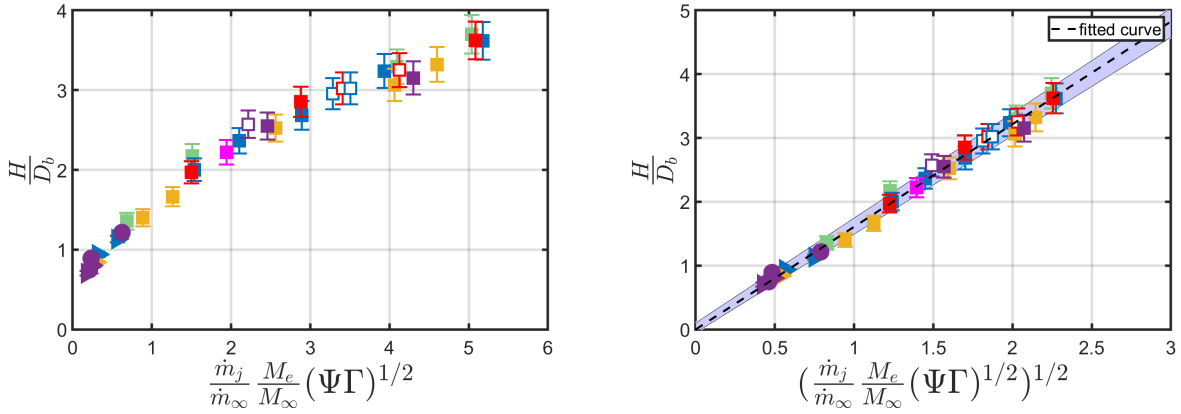

(a) (b)

Figure 5.11: Results of using modified mass flow rate ratio (Ξ) as a scaling law for bow shock standoff distance. Fitted curve represented by $y = 1.593 + 0.025$.

5.2.6 Discussion of differences between these two scaling parameters

Further comparison between the results from the current study and those from previous experiments were conducted to test the generality of the proposed scaling laws and identify their differences. Results from Romeo and Sterret [1] and Gutsche et al [7] were chosen due to similarities between their retronozzle geometries and those used in the current study. Key differences between the test conditions used by the three datasets can be visualized when looking at Figure 5.12. Romeo and Sterret conducted tests at $M_\infty = 6$ and M_e ranging between 1 and 3.5, while Gutsche et all used M_∞ values between 5.3 and 7 and M_e values between 2.1 and 2.5. Converting these values to Mach number ratio results in ranges between 0.16 and 0.58 for Romeo and Sterret and 0.31 to 0.46 for Gutsche et al.

It is possible that the lack of Mach number dependence observed by Gutsche is due to the relatively small variation in Mach number ratio throughout their dataset. Additionally, the nozzle internal structure used in Gutsche et al differed from those in the current study and that of Romeo and Sterret by using a contoured nozzle rather than a conical one. This variation may also play a role in Mach number dependence through the divergence angle present at the exit plane of the nozzle.

Both ranges are far below the ratios used in the current study of 1 and 1.5. To visually identify the variations in Mach number ratio within each dataset, a gradient was applied where lighter indicates a higher Mach number ratio and darker indicates a lower Mach number ratio. Error bars from these datasets were unavailable.

Results of the two candidate scaling laws presented earlier are expanded to include the additional datasets in Figure 5.13. The modified mass flow rate parameter collapses the data better than C_{TM}. This result supports the argument presented earlier that C_T scaling is a function of Mach number for both the freestream and retrojet. However, it indicates that M_e/M_∞ may not be the correct term when hypersonic Mach numbers are reached due to the poor collapse for Figure 5.13b. Further investigation into the mathematical differences between the scaling laws may help identify mechanisms for this poor collapse.

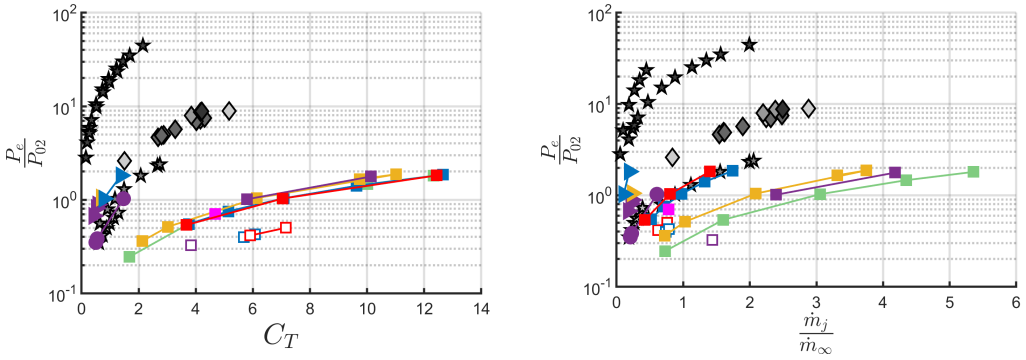

(a) (b)

Figure 5.12: Parameter space when Romeo and Sterret [1] (stars) and Gutsche et al [7] (diamonds) results are included. Semilog plots were needed due to the extremely high pressure ratios reached by [1] and [7] indicative of higher M_∞ values. (Results from Romeo and Sterret courtesy of Korzun and Cassel [3]).

Neither candidate scaling law is equivalent in magnitude. The difference between C_{TM} and Ξ can be mathematically defined in the following steps. Equation 5.1 shows that after combining terms, Ξ can be simplified to be a function purely of Mach number, area ratio, pressure, and ratio of specific heat.

$$\Xi = \frac{\rho_j V_j A_e}{\rho_\infty v_\infty A_b}\frac{M_e}{M_\infty}\Psi\Gamma = \frac{M_e^2}{M_\infty^2}\frac{A_e}{A_b}\frac{P_j}{P_{0,j}}\frac{P_{0,\infty}}{P_\infty}\frac{P_{0,j}}{P_{0,\infty}}\sqrt{\frac{T_\infty}{T_{0,\infty}}}\sqrt{\frac{T_{0,j}}{T_j}} \tag{5.1}$$

Expanding thrust coefficient in a similar way shows a similar dependence.

$$C_T = \frac{\tau}{q_\infty A_b} = \frac{2(\dot{m}_j u_j + A_e P_j)}{\rho_\infty {u_\infty}^2 A_b} = \frac{2(1+\gamma_j M_e^2)}{\gamma_\infty M_\infty^2}\frac{A_e}{A_b}\frac{P_j}{P_\infty} = \frac{2(1+\gamma_j M_e^2)}{\gamma_\infty M_\infty^2}\frac{A_e}{A_b}\frac{P_j}{P_{0,j}}\frac{P_{0,\infty}}{P_\infty}\frac{P_{0,j}}{P_{0,\infty}} \tag{5.2}$$

Multiplying thrust coefficient by the Mach number ratio results in C_{TM}.

$$C_{TM} = \frac{2(1+\gamma_j M_j^2)}{\gamma_\infty M_\infty^2}\frac{A_e}{A_b}\frac{P_j}{P_{0,j}}\frac{P_{0,\infty}}{P_\infty}\frac{P_{0,j}}{P_{0,\infty}}\frac{M_e}{M_\infty} \tag{5.3}$$

These two terms (Ξ and C_{TM}) can be related by multiplying the scaled mass term by the

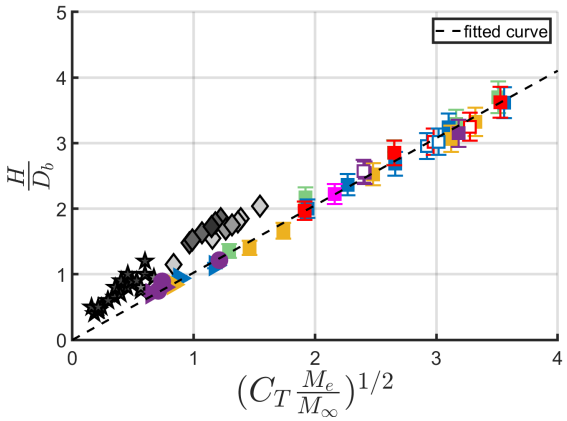

(a)

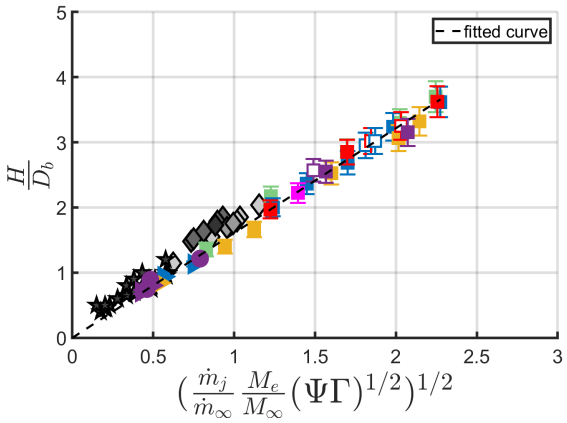

(b)

Figure 5.13: C_{TM} (a) and modified mass flow rate ratio (b) scaling laws including data from Romeo and Sterret (1963) (stars) and Gutsche et al (2021) (diamonds) [1][7] . Fitted curves remain unchanged from section 5.2.6.

Mach number ratio, temperature iscentropic relations, and a function of both Mach number and γ. Together these terms are grouped into a coefficient represented by C_0.

$$C_{TM} = (\Xi)\frac{2(1+\gamma_j M_e^2)}{\gamma_\infty M_\infty^2}\frac{M_\infty}{M_e}\sqrt{\frac{T_{0,\infty}}{T_\infty}}\sqrt{\frac{T_j}{T_{0,j}}} \tag{5.4}$$

$$C_{TM} = \Xi C_0 \tag{5.5}$$

The term C_0 is purely a function of the freestream and retrojet Mach numbers and ratios of specific heat. Influences of these variables on C_0 are shown in Figure 5.14. When Mach numbers and ratios of specific heats are matched between the two flows, C_0 can be represented as an inverted rational function whose value asymptotes to 2 as the values of M_e and M_∞ approach infinity (dashed black curve). Additionally, curves representing how C_0 changes with respect to M_e given a constant value of M_∞ are plotted. These curves all use γ_j and γ_∞ values equivalent to air (1.4). Values for C_0 from the dataset collected for this thesis (green) were also plotted and compared against values taken from Romeo and Sterret [1] shown in blue and Gutsche et al (2021) shown in red [7]. The cluster of green points around $M_e = 2$ shows minimal influence from changes in γ_j and γ_∞ on C_0 even with the He and CO_2 gas data. M_∞, within the range of values presented, is the biggest influence on the value of C_0 with this effect diminishing as M_∞ approaches hypersonic values. Similarly the influence of M_e also diminishes as M_∞ approaches hypersonic speeds. This trend may help explain why Gutsche et al did not observe a Mach number dependence in their results given their hypersonic test conditions.

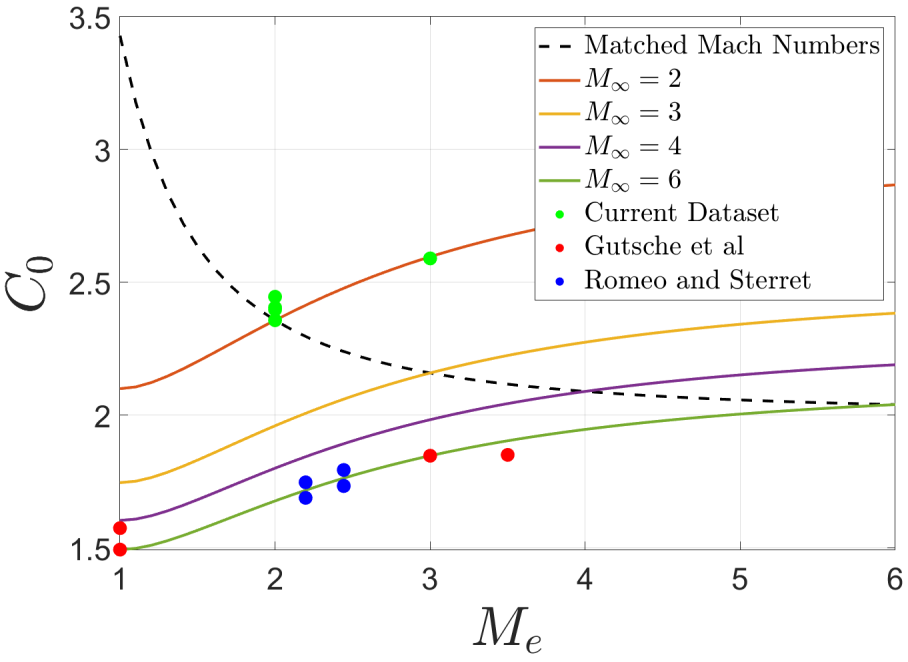

Figure 5.14: Curves displaying how coefficient C_0 changes due to influence from M_e for various freestream mach numbers where γ_j and γ_∞ are both 1.4. Values for C_0 from various datasets are also included.

Chapter 6

CONCLUSION

For this thesis, the scaling of shock standoff distance and bow shock curvature with respect to various thermodynamic and geometric variables was studied for SRP flows. The capabilities of the retropropulsion experimental apparatus at the University of Washington was expanded to use various gasses in the retrojet and freestream flows at a range of temperatures. New test articles, nozzles, and gas tubing systems were created in addition to a gas heater and control unit. Having completed these tasks, a unique dataset of heated and unheated SRP interactions using a variety of gas combinations, Mach numbers, and test article geometries was compiled.

The results obtained from the dataset helped test existing hypotheses around stability predictions for SRP flowfields. Values for $P_e/P_{0,2}$ where the flowfield was stable were found to be significantly below unity and were shown to be highly dependant on forebody geometry and jet exit Mach number, contradicting results presented in the literature. The relationship between expansion conditions of the jet, gas composition, and stability of the flowfield was not explored further in this thesis, but are presented in Jones (2022) [8]. It remains unclear whether the expansion conditions of the jet are indicative of flowfield stability or if relative values of $P_e/P_{0,2}$ inaccurately predict expansion conditions [8].

The addition of shock radius of curvature as a geometric scaling variable for analyzing SRP flowfields shows distinctly similar results to that of shock standoff distance. Further investigation of the relationship between these two measured values show that the bow shock shape is approximately self-similar regardless of freestream or retrojet gas composition. In addition, results indicate that jet exit Mach number may appear to weakly influence the shock radius of curvature relative to standoff distance. Caveats for using shock radius of

curvature include the parameter's sensitivity to small perturbations, giving results obtained using shock standoff distance a comparatively higher degree of confidence.

Thrust coefficient (C_T) is shown to collapse shock standoff distance regardless of gas composition or temperature and only shows dependence on jet exit Mach number, contradictory to results presented in Gutsche et al [7] who used single-gas, constant temperature conditions at hypersonic freestream speeds. Jet exit Mach number dependence seen in the results presented agrees, however, with results from Jarvien and Adams [14] as well as Romeo and Sterret [1]. The ratio of jet exit to freestream Mach number was shown to collapse C_T results on a single curve. Possible causes for the contradictory results between hypersonic and supersonic freestream conditions may be the result of geometric variations between those used in this thesis and that of Gutsche et al. Contoured vs conical nozzle construction may play a key role in the development of the plume shock region and in turn affect the overall flowfield. Separately, a decreasing dependence on Mach number as conditions move into the hypersonic regime may be influencing this result as well. It is possible that the analysis presented using a control volume similar to that of Finley (1966) may define a parameter that accounts for this change, but would require updated assumptions for more accurate results.

Mass flow rate ratio scaling was also investigated using terms suggested by the mass conservation control volume in Korzun and Cassel (2020). Results show that explicit functions of molecular weight, temperature and ratio of specific heats in addition to Mach number ratio can collapse shock standoff distance quite well.

Further comparison between the two scaling laws was achieved using data from Romeo and Sterret (1963) and Gutsche et al (2021) who used similar geometric test articles to those used in this thesis. Analysis shows that Mach number effects drastically influence the relative difference between these scaling laws with C_0 having an inverse relationship with M_∞, and a positive relationship with M_e. These effects diminish however as M_∞ reaches hypersonic speeds. The inclusion of these results suggests that mass flow rate scaling has an improved collapse over C_T and is a better predictor of shock standoff distance, however the difference is not large. This conclusion appears to hold regardless of freestream or jet exit Mach number

as well as thermodynamic and geometric parameters.

REFERENCES

[1] Romeo, D. J. and Sterrett, J. R., *Exploratory investigation of the effect of a forward-facing jet on the bow shock of a blunt body in a Mach number 6 free stream*, National Aeronautics and Space Administration, 1963.

[2] Korzun, A. M., Braun, R. D., and Cruz, J. R., "Survey of supersonic retropropulsion technology for Mars entry, decent and landing," *Journal of Spacecraft and Rockets*, Vol. 46, 2009, pp. 929–937.

[3] Korzun, A. M. and Cassel, L. A., "Scaling and Similitude in single nozzle supersonic retropropulsion aerodynamics interference," *AIAA 2020-0039*, 2020.

[4] Finley, P., "The flow of a jet from a body opposing a supersonic free stream," *Journal of Fluid Mechanics*, Vol. 26, No. 2, 1966, pp. 337–368.

[5] Yang, X., *Influence of jet pressure on multi-nozzle supersonic retropropulsion flowfields*, Master's thesis, University of Washington, 2019.

[6] Ho, B., *Characterizing unsteadiness in supersonic retropropulsion flows*, Master's thesis, University of Washington, 2019.

[7] Gutsche, K., Marwege, A., and Gülhan, A., "Similarity and Key Parameters of Retropropulsion Assisted Deceleration in Hypersonic Wind Tunnels," *Journal of Spacecraft and Rockets*, 2021, pp. 1–13.

[8] Jones, L., *Characterization of Onset and Transition to Instability in Supersonic Retropropulsion*, Master's thesis, University of Washington, 2022.

[9] Tan, Y. M., *Influence of Pressure on Supersonic Retropropulsion Flow Field at Mach 2*, Master's thesis, University of Washington, 2018.

[10] NASA, "NASA Technology Roadmaps - TA 9: Entry, Descent, and Landing," Tech. rep., National Aeronautics and Space Administration, 2015.

[11] Edquist, K. T., Korzun, A. M., Dyakonov, A. A., Studak, J. W., Kipp, D. M., and Dupzyk, I. C., "Development of supersonic retropropulsion for future mars entry, descent, and landing systems," *Journal of Spacecraft and Rockets*, Vol. 51, No. 3, 2014, pp. 650–663.

[12] Edquist, K., Dyakonov, A., Korzun, A. M., Shidner, J. D., Studak, J. W., Tigges, M. A., Kipp, D. M., Prakash, R., Trumble, K. A., and Dupzyk, I. C., "Development of supersonic retro-propulsion for future Mars Entry, Descent and Landing systems," *AIAA 2010-5046*, 2010.

[13] Korzun, A. M. and Bibb, K. L., "Powered Descent Aerodynamics for Low and Mid Lift-to-Drag Human Mars Entry, Descent, and Landing Vehicals," *AIAA 2020-0039*, 2020.

[14] Jarvinen, P. and Adams, R., "The Aerodynamic Characteristics of Large Angled Cones with Retrorockets," 1970.

[15] Barber Jr, E. A., "An experimental investigation of stagnation-point injection," *Journal of Spacecraft and Rockets*, Vol. 2, No. 5, 1965, pp. 770–774.

[16] Pindzola, M., "Jet simulation in ground test facilities," Tech. rep., ADVISORY GROUP FOR AERONAUTICAL RESEARCH AND DEVELOPMENT PARIS (FRANCE), 1963.

[17] Berry, S., Rhode, M., and Edquist, K., "Supersonic retropropulsion validation experiment in the NASA Langley unitary plan wind tunnel," *Journal of Spacecraft and Rockets*, Vol. 51, 2014.

[18] Bergman, T., Incropera, F., DeWitt, D., and Lavine, A., *Fundamentals of Heat and Mass Transfer*, Wiley, 2011.

Appendix A

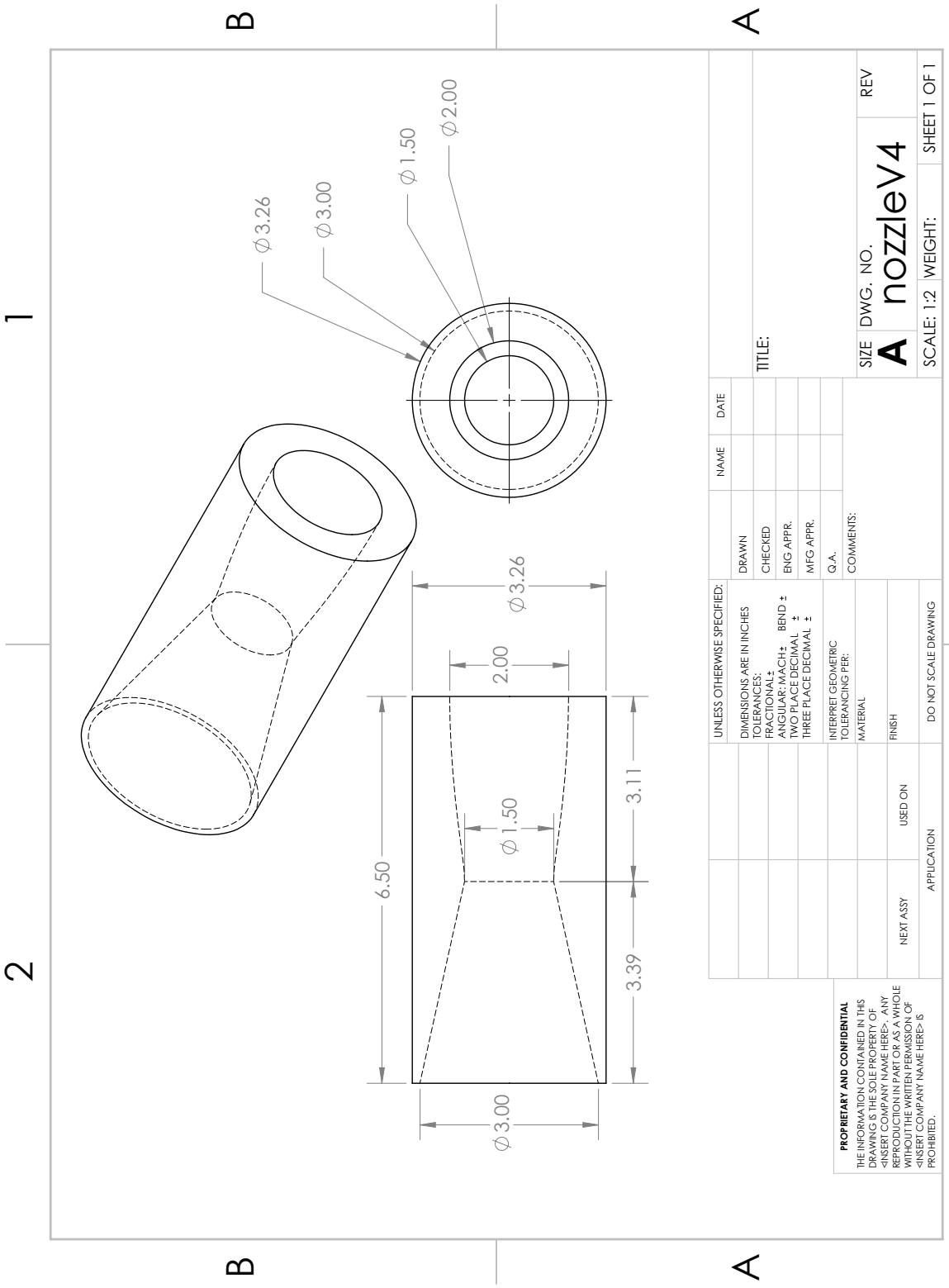

Figure A.1: Mach 2 freestream nozzle for Ludwig tube designed by Jones [8]($\gamma = 1.28$).

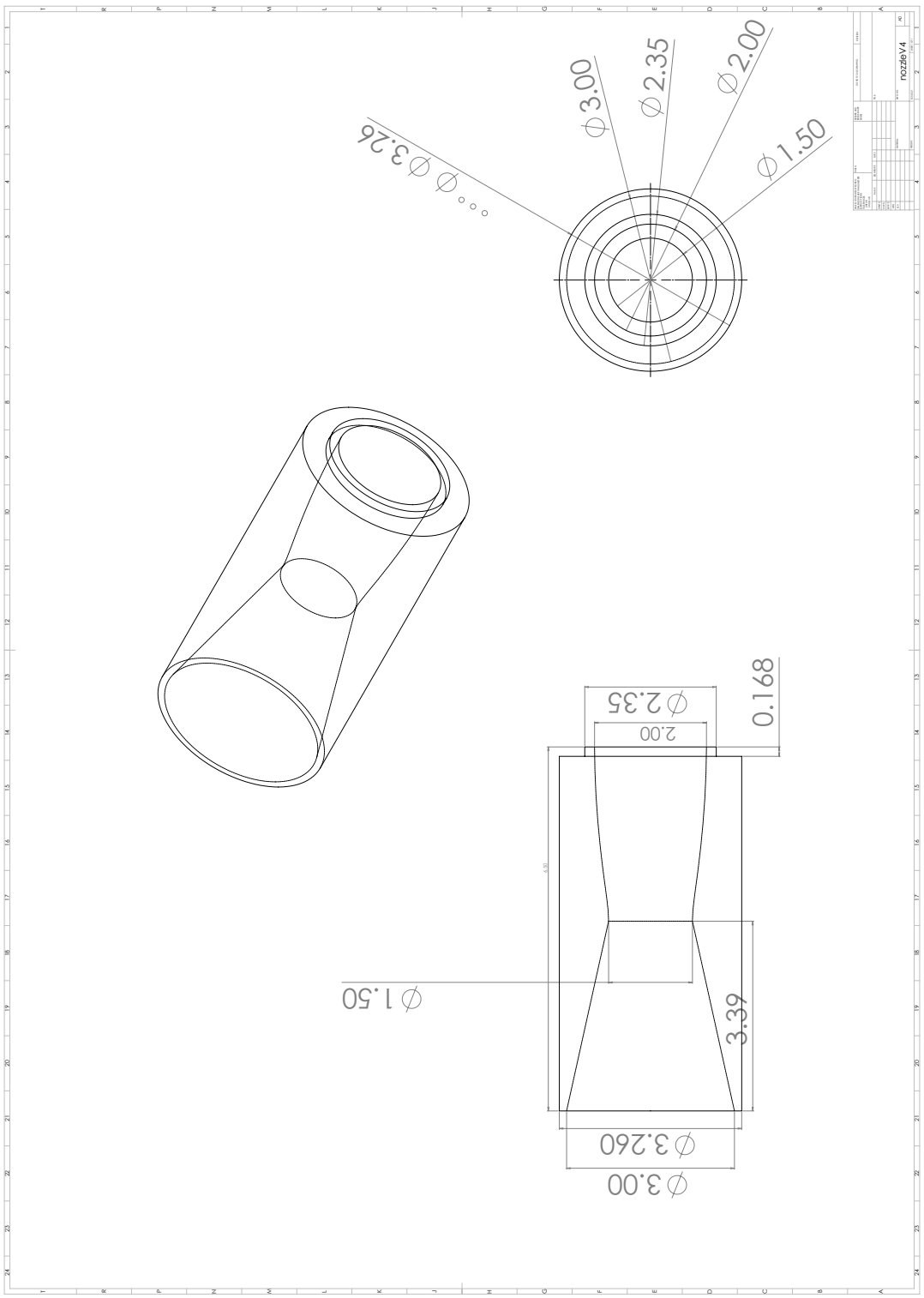

Figure A.2: Mach 2 freestream nozzle for Ludwig tube designed by Tan [9]($\gamma = 1.4$).

Appendix B

	Matched Values	M_e	Gas Composition	Psi	Gamma	D_b/D_e
$\frac{P_e}{P_{0,2}}$	0.52 ± 0.02	2	$CO_2 - Ar$	1.15	1.29	1.52
			$CO_2 - N_2$	1.63	1.09	1.52
			$CO_2 - He$	11.43, 16.81 ± 0.5	1.29	1.52
	1.1 ± 0.01	2	$CO_2 - Ar$	1.15	1.29	1.52
			$CO_2 - N_2$	1.63	1.09	1.52, 4.57
			$CO_2 - He$	11.43, 16.81 ± 0.5	1.29	1.52, 4.57
			$N_2 - N_2$	1.06	1.0	1.52, 4.57
	1.81 ± 0.02	2	$CO_2 - Ar$	1.15	1.29	1.52
			$CO_2 - N_2$	1.63	1.09	1.52
			$CO_2 - He$	11.43, 16.81 ± 0.5	1.29	1.52, 3.05
			$N_2 - N_2$	1.06	1.0	1.52
C_T	3.9 ± 0.2	2	$CO_2 - Ar$	1.15	1.29	1.52
		2	$CO_2 - He$	11.43, 16.81 ± 0.5	1.29	1.52
		3	$N_2 - N_2$	1.06	1.0	1.52
	6 ± 0.2	2	$CO_2 - N_2$	1.63	1.09	1.52
		3	$CO_2 - He$	11.43, 16.81 ± 0.5	1.29	1.52
		3	$N_2 - N_2$	1.06	1.0	1.52
	10 ± 0.4	2	$CO_2 - Ar$	1.15	1.29	1.52
			$CO_2 - N_2$	1.63	1.09	1.52
			$CO_2 - He$	11.43	1.29	1.52
$\frac{\dot{m}_j}{\dot{m}_\infty}$	0.75 ± 0.02	2	$CO_2 - Ar$	1.15	1.29	.125
		2	$CO_2 - N$	1.63	1.09	1.52
		2, 3	$CO_2 - He$	11.43, 16.81 ± 0.5	1.29	1.52
		2	$N_2 - He$	7.40	1.19	1.52

Table B.1: Caption